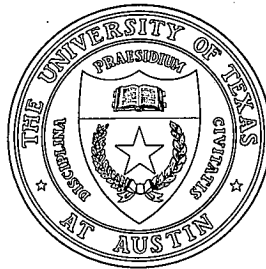# INSTITUTE FOR
FUSION STUDIES

Instabilities and Vortex Dynamics
in Shear Flow of Magnetized Plasmas

T. Tajima, W. Horton, P. J. Morrison, J. Schutkeker,
T. Kamimura, K. Mima, and Y. Abe

Institute for Fusion Studies
The University of Texas at Austin
Austin, Texas 78712

March 1990

THE UNIVERSITY OF TEXAS

AUSTIN

Instabilities and Vortex Dynamics in Shear Flow of Magnetized Plasmas

T. Tajima, W. Horton, P. J. Morrison, J. Schutkeker
T. Kamimura, K. Mima, and Y. Abe
Institute for Fusion Studies
The University of Texas at Austin
Austin, Texas 78712

Abstract

Gradient-driven instabilities and the subsequent nonlinear evolution of generated vortices in sheared $\mathbf{E} \times \mathbf{B}$ flows are investigated for magnetized plasmas with and without gravity (magnetic curvature) and magnetic shear by using theory and implicit particle simulations. In the linear eigenmode analysis, the instabilities considered are the Kelvin-Helmholtz (K-H) instability and the resistive interchange instability. The presence of the shear flow can stabilize these instabilities. The dynamics of the K-H instability and the vortex dynamics can be uniformly described by the initial flow pattern with a vorticity localization parameter ϵ. The observed growth of the K-H modes is exponential in time for linearly unstable modes, secular for marginal mode, and absent until driven nonlinearly for linearly stable modes. The distance between two vortex centers experiences rapid merging while the angle θ between the axis of vortices and the external shear flow increases. These vortices proceed toward their overall coalescence, while shedding small-scale vortices and waves. The main features of vortex dynamics of the nonlinear coalescence and the tilt or the rotational instabilities of vortices are shown to be given by using a low dimension Hamiltonian representation for interacting vortex cores in the shear flow.

1

I. Introduction

The presence of shear in the flow of neutral fluids and plasmas gives rise not only to instability of the sheared layer, i.e., the Kelvin-Helmholtz (K-H) instability, but also to stabilization of other instabilities, the interchange mode [Rayleigh-Taylor (R-T) instability] for instance. Resistive interchange driven turbulence has been proposed as a mechanism for the anomalous thermal transport in stellarators and in edge plasmas of tokamaks. Recent calculations indicate that a strong nonuniform radial electric field can suppress the interchange[1] and resistive pressure-gradient-driven instabilities.[2] The fluid dynamics of shear flows under the influence of gravity is also important for the problem of an imploding inertially confined plasma. In the initial phase of implosion, short wavelength modes are stabilized by the ablative flow and relatively long wavelength modes can grow on an ablation surface.[3,4] Large-scale vortices excited by the R-T instability are adiabatically compressed, and thus increase in strength during the implosion. It appears that the shear flows associated with large scale-length vortices suppress the short wavelength R-T mode in the stagnation phase that occurs during the final phase of the implosion. The presence of vortices can also influence the nature of turbulence and associated transport. In the isotropic 2-D Navier-Stokes turbulence the well-known Kolmogorov power spectrum of k^{-3} develops from space filling small-scale eddies. However, we find that the turbulence power spectrum changes to a steeper power law in k in the presence of vortical structure in the fluid in the wavenumber regime on the scale of the vortices. Thus the presence and dynamics of the vortices may strongly affect the macroscopic behavior of turbulence.

In this work, we extend the previous work[5] by investigating the shear flow effects on the gravitational instability and the magnetic shear effects on the K-H and R-T instabilities. Also, the detail analysis of the nonlinear evolution of large size vortices is presented here.

In magnetic confinement devices the shear flow occurs at the boundary between the rotating core plasma and the stationary edge plasma. The magnitude and direction of

the core rotation is determined by the strength of the nonambipolar loss rates leading to the charge up of the plasma. The mirror or open field line confinement system has an intrinsically faster electron loss rate leading to the net positive potential of several times the electron temperature. In the stellarator with strong electron cyclotron heating there is also a dominant electron loss and positive charge to the plasma. In contrast, for stellarators with neutral beam injection or ion cyclotron heating and in general for tokamaks, there is a net radial ion loss rate from finite ion orbits size effects and the plasmas build up a substantial, of order the ion temperature, negative potentials. The positive potential plasmas rotates in the ion diamagnetic direction and the negative potential plasmas in the electron diamagnetic direction. In typical stability analysis the assumption is made that the rotation is sufficiently close to a solid body rotation and sufficiently slow that the only effect is to Doppler shift the wave frequencies from the values calculate in the absence of rotation. The conditions for the limit of this approximation are given in Ref. 1 for the rotating cylindrical plasma with ω_{*e} and ω_{*i} drift modes. In the presence of shear flow we can estimate the condition for a strong effect of the shear flow on a mode of growth rate γ_{k_y}, wavenumber k_y and mode width Δx by the condition

$$k_y \Delta x u' > \gamma_{k_y}.$$

Applying this condition to the values of k, Δx, γ_k for the interchange, resistive g and the drift wave gives a first estimate for the shear flow required to reduce the growth rate. Table I shows the condition on u' obtained from this criterion for several forms of plasma turbulence.

Since the sheared velocity flow contains a source of free energy one expects instability to arise from the shear flow which it does above a critical strength. However, the forms of the eigenmodes of the K-H are sufficiently different from those of the interchange-drift wave type of instability that there is generally a substantial window between the stabilizing effect of the shear flow on the interchange modes and the onset of the Kelvin-Helmholtz instability as shown in some detail for the $m = 1$ and 2 modes of the rotating cylinder in Ref. 1.

3

Recent experiments[6] in the DIII-D tokamak show that associated with L (low) to H (high) confinement mode transition, there is a substantial increase in the perpendicular component of the plasma flow velocity as measured by the spectroscopic shifts of helium line radiation.[7] No such appreciable change is observed in the toroidal component of the plasma flow velocity. Taylor et al.[8] also report no appreciable change in the toroidal velocity and a substantial increase in the poloidal velocity with the onset of H-mode-like plasma conditions. The abrupt change in the flow speed is interpreted to be due to a strengthening of the radial electric field strength. Shaing and Crume[9] has interpreted this change in the radial field strength with increased nonambipolar radial ion currents and a bifurcation to a new rotational equilibrium.

Shaing[2] notes that without considering the stability problem there may arise improved confinement due to the shear flow layer. Biglari et al.[10] also discuss that the shear flow in itself may reduce the transport. A simple single mode description of the shear flow reduction in transport is given by the convective cell island width formula[1]

$$\Delta r = 2 \left[\frac{c\tilde{\varphi}}{rB|d\Omega/dr|} \right]^{1/2} ,$$

which traps plasma to form an insulating layer. Here Ω is the poloidal rotation rate $\Omega = (c/rB)(d\Phi/dr)$ and $\tilde{\varphi}$ the amplitude of the vortex wave.

In the present work we consider how the shear flow may strongly modify the strength of the growth rates of the underlying turbulence generation from the interchange and drift wave types of instabilities. Theilhaber and Birdsall[11] studied the K-H instability with finite Larmor radius effects fully taken into account but without magnetic shear effect. Such a treatment may be applicable when the shear flow region is very narrow and in the current free region near the wall of the tokamak or stellarator.

A similar charge separation induced shear flow appears in the Barium ion injection in the ionosphere.[12] Other magnetospheric appearances[13] and astrophysical ones such as jets[14] of the shear flow instability are noted. When the shear flow is sufficiently strong to dominate the stabilizing effects of magnetic shear, the growth rate reaches a maximum for wavenumber

$k_y \simeq 1/2a$ where the maximum growth rate is $\gamma_{\max} \simeq 0.2 \max |dv_y/dx| \simeq 0.2u/a$. Since the short wavelength modes with $k_y a > 1$ are stable to exponential growth, vortices excited by the K-H instability extend over all the shear flow region with $\lambda_x \sim \lambda_y > a$. When the shear flow dominates, the density and temperature fields are passively convected with the fluctuations characterized by $e\varphi/T_e \gg \delta n/n$, $\delta T/T$.

The fastest growing normal mode forms a perturbed vortical flow pattern with the axis of the vortex tilted with respect to the flow direction, as shown by theory[1] and simulation.[5] The tilting of the vortical flow produces a momentum flux $\pi = \langle v_x v_y \rangle$ across the shear layer. The momentum flux takes energy out of the shear and puts it into the vortical flows. Subsequently the vortices coalesce, with the dominant wavelength shifting to a multiple of the original wavelength. This shifting to longer wavelengths is a configuration space representation of the inverse cascade. Often the coalescing vortices or islands persist for long times.

The effect of the electron parallel motion on stabilization of the K-H mode is shown to reduce the maximum growth rate. The electron density fluctuations induced by the electron parallel motion $\left(\nabla_\parallel \cdot \mathbf{j}_\parallel \right)$ balance with the ion density fluctuations generated by the ion perpendicular motion $(\nabla_\perp \cdot \mathbf{j}_\perp)$. Namely, for charge neutral currents we have

$$\nabla_\perp \cdot \mathbf{j}_\perp + \nabla_\parallel \cdot \mathbf{j}_\parallel = 0.$$

Since $j_\parallel \sim \eta E_\parallel = -ne^2 \nabla_\parallel \phi / m\nu_{ei}$, $\mathbf{j}_\perp \sim -\frac{d}{dt}\frac{ne\nabla_\perp \phi}{B\omega_{ci}}$ from the ion inertia current. The effect of the electron parallel motion is significant when

$$\frac{k_\parallel^2 v_e^2}{\nu_{ei}} \gtrsim k_\perp^3 u \rho_s^2.$$

Here ν_e is the electron thermal velocity, ν_{ei} is the electron-ion collision frequency, ϕ the fluctuation potential, ω_{ci} the ion cyclotron frequency, ρ_s the ion inertial gyroradius, and u is the velocity spread in the $E \times B$ drift velocity. For a K-H mode with $k_\perp \lesssim 1/a$ the critical tilt angle θ_c, as measured between the $\mathbf{k}$ vector and the ambient magnetic field, is

given by $\theta_c \simeq \frac{\rho_s}{a}\left(\frac{u}{v_e}\frac{a}{l_e}\right)^{1/2}$, where l_e the mean free path of electrons. For $\theta \gtrsim \theta_c$, the K-H instability will be stabilized. In the case of a sheared magnetic field, the tilt angle $\theta \simeq a/L_s$ is produced by the shearing of the magnetic field with L_s being the shear length. Therefore, the K-H mode is significantly stabilized when $L_s \lesssim (a^2/\rho_s)(l_e v_e/ua)^{1/2}$. The ratio of the parallel diffusion $k_\parallel^2 v_e^2/\nu_{ei}$ to the ion inertial acceleration $k_\perp^2 \rho_s^2 k_y u$ is sometimes called R as is given by $R = k_y v_e^2 \Delta x^4/\nu_{ei} u \rho_s^2 L_s^2$. Both the resistive g and the K-H growth rates decrease with increasing R.

When there exist a density gradient and a gravity force as shown in Fig. 1, the interchange modes can be unstable. Here we use gravity to represent either the effective acceleration from the ∇B curvature drift of the ions or the acceleration during implosion. The maximum growth rate for the density gradient $\frac{d\ln n_0}{dx} \equiv 1/L_n$ and the gravity $g \simeq v_i^2/R$, where v_i is the ion thermal velocity and R the major radius of tokamak, is $\sqrt{g/L_n}$.

When there is a shear flow with $|dv_y/dx| \simeq u/a$, the interchange mode can be stabilized. Stabilization by the velocity shear occurs when $u/a > \sqrt{g/L_n}$.

Let us give two examples for the above instabilities. The first example is an edge plasma of the TEXT tokamak.[8] The shear flow layer width $a \sim 1$ cm, the velocity $u \simeq 3 \times 10^5$ cm/sec up to 10^6 cm/s, the electron temperature $T_e \simeq 20$ eV, the density $n_0 \simeq 2 \times 10^{12}$/cm^3, the density scale length $L_n \simeq 3$ cm and the magnetic field curvature $R \gtrsim 1$ m. The electron mean free path $l_e \sim 200$ cm and the hybrid ion gyroradius $\rho_s \simeq 0.1$ cm for the above parameters. If the magnetic shear length $L_s \gtrsim 25$ m, the K-H modes are unstable. In this case, the parallel wavelength is about 10 m. As for the interchange instability, the flute mode is stabilized by the strong shear flow, since $u/a \simeq 3 \times 10^5$/sec $\gtrsim \sqrt{g/L_n} \approx 2 \times 10^5$/sec.

The second example is the Rayleigh-Taylor instability of the imploded laser plasma. A typical acceleration rate gives $g \simeq c_s^2/\Delta R$ for the target shell thickness ΔR. The velocity shear will be given by $\alpha c_s/\Delta R$. Since the Rayleigh Taylor mode growth rate is $\sqrt{kg}$, the

stability criteria is roughly given by

$$\alpha c_s / \Delta R \gtrsim 2\sqrt{k c_s^2 / \Delta R}.$$

Therefore, the unstable modes are limited to short wavelengths where $k \lesssim \alpha^2/4\Delta R$, and $\alpha \gtrsim 1$ will strongly stabilize the Rayleigh Taylor instability.

The characteristic time scale of the Kelvin-Helmholtz or interchange processes do not involve a characteristic oscillation frequency, such as the plasma, cyclotron or the ion acoustic frequencies, in the center of mass frame of the plasma. The plasma flow is due to the $E \times B$ drift of the guiding centers and the characteristic time scales are those of hydrodynamic flows, although the elementary process is that of a magnetized plasma with long range Coulomb interactions. The effects of finite pressure density gradient and gravity, across the magnetic field and the shear flow layer, bring in the drift wave frequencies ω_{*e} and ω_{*pi}. Thus to study the nonlinear evolution of shear flows and vortices associated with the magnetized plasma through numerical simulation, time scales much longer than the plasma oscillation periods are required. We employ the implicit simulation technique[15] which systematically removes the characteristic time scales and spatial length scales that are smaller than the time step Δt and space scales Δx chosen for the space-time grid. The filtering method has been shown to preserve the accuracy for the low-frequency ($\omega \Delta t \ll 1$) dynamics.[16]

In the present article we investigate the nonlinear evolutions of the Kelvin-Helmholtz and interchange instabilities as an initial value problem through particle simulation, in contrast to the previous work[5] where the shear flow was externally fixed with an imposed driver, as would arise from nonambipolar losses in the background plasma. The secular growth and decay of the marginally stable normal modes are also studied. After the linear stage of exponential growth of the primary normal modes, the growth of secondary modes can be nonlinearly triggered.

In order to systematically explore the parametric dependence of the development in the nonlinear stage, we isolate the evolution of vortex coalescence and associated processes caused

7

by vortex formation, which in turn is due to the K-H instability and its nonlinear evolution. To investigate the second stage, the system is initiated from the secondary equilibrium of a chain of finite amplitude vortices. The chain of vortices is unstable against the coalescence mode and against the tilt or rotational mode. In this nonlinear regime the growth of coalescence and tilt modes are nonlinear instabilities showing the finite time singularity like $(t_c - t)^{-\alpha}$ for times $t \lesssim t_c$.

In Sec. II the equations for K-H and interchange instabilities, both for plasmas with and without a magnetic field are derived. These equations include the effects of velocity shear, magnetic shear, density gradients, gravity, and electron-ion collisions. The linear dispersion relations derived from the equations for the two instabilities are also discussed in two analytic limits. In Sec. III we study the initial value simulation of the shear flow K-H instabilities, both in its linear and nonlinear stages. In Sec. IV the nonlinear evolution of vortices, starting from the periodic chain of vortices, is examined and the coalescence and tilt instabilities of vortices are studied via the particle simulation method. Theoretical modeling of these processes is presented in Sec. V and compared with the simulation experiments of Sec. IV. In Sec. VI we summarize the results and discuss the applications of the results to fusion plasmas.

II. Vortex Equation in a Plasma with Velocity Shear, Magnetic Shear, Gravity, and Density Gradient: K-H and Interchange Stability Analysis

We carry out linear theoretic analysis of plasma stability associated with shear flows. We consider the effects of shear flows and gravity both in magnetized and unmagnetized plasmas. In the case of a magnetized plasma, the static sheared magnetic field is given by $\mathbf{B}_0 = B_0 (\hat{z} + \hat{y} x / L_s)$, which is shown in Fig. 1. The initial ion density has a gradient of $1/L_n =$

$\partial \ln n_0 / \partial x$ between $x = b$ and $-b$. The flow velocity is in the y-direction, and changes according to

$$\mathbf{v}_0 = \begin{cases} u & x > a \\ u(x/a) & |x| < a \\ -u & x < -a. \end{cases}$$

The geometry is schematically shown in Figs. 1a and b. Except for especially indicated cases, we consider the above plasma geometry. Also, gravity is applied in the x-direction, which destabilizes (stabilizes) the interchange mode for $\gamma_g^2 = g/L_n \gtrless 0$.

In the case of low-frequency modes with relatively long wavelengths $\lambda \gg \lambda_{De}$, where λ_{De} is the electron Debye length, the condition of charge neutrality can be assumed. Namely,

$$n_i = n_e = n. \tag{1}$$

From the electron equation of motion along $\mathbf{B}$, we obtain the equation for the parallel electron current $j_{\parallel}$

$$m_e \left(\frac{\partial}{\partial t} + \mathbf{v}_E \cdot \nabla \right) j_{\parallel} = -ne^2 \nabla_{\parallel} \phi + e \nabla_{\parallel} p_e - m_e \nu_e j_{\parallel} \simeq 0, \tag{2}$$

where $\mathbf{v}_E$ is the $\mathbf{E} \times \mathbf{B}$ drift, ϕ is the electrostatic potential perturbation, p_e is the electron pressure, and ν_{ei} is the effective electron collision frequency. Using the electron equation of continuity and Eq. (2), we obtain

$$\left(\frac{\partial}{\partial t} + \mathbf{v}_E \cdot \nabla_{\perp} \right) n_e = \frac{1}{e} \nabla_{\parallel} \cdot \mathbf{j}_{\parallel}$$

$$= \frac{1}{m \nu_{ei}} \left(-n_0 e \nabla_{\parallel}^2 \phi + \nabla_{\parallel}^2 p_e \right). \tag{3}$$

Assuming T_e constant and $n_e = n_0(x) \left(1 + \tilde{n}_e \right)$ Eq. (3) is rewritten as

$$\left(\frac{\partial}{\partial t} + \mathbf{v}_E \cdot \nabla \right) \tilde{n}_e = \frac{c_s \rho_s}{L_n} \frac{\partial \tilde{\phi}}{\partial y} + \frac{v_e^2}{\nu_{ei}} \nabla_{\parallel}^2 \left(\tilde{n}_e - \tilde{\phi} \right), \tag{4}$$

where $\tilde{\phi} = e\phi/T_e$, $L_n = |d \ln n_0/dx|^{-1}$, $c_s = \sqrt{T_e/M_i}$, and $\rho_s = c_s/\omega_{ci}$, where ω_{ci} is the ion cyclotron frequency. In Eq. (4), nonlinearities other than the nonlinear polarization drift are neglected.

9

From the ion equation of motion, we obtain $\mathbf{v}_{i\perp}$, the ion drift velocity perpendicular to the magnetic field

$$\mathbf{v}_{i\perp} = \mathbf{v}_E + \mathbf{v}_g + \mathbf{v}_d + \mathbf{v}_p, \tag{5}$$

where

$$\mathbf{v}_E = \frac{\hat{\mathbf{z}} \times \nabla (\phi_0 + \phi)}{B_0} c, \tag{6}$$

$$\mathbf{v}_g = \frac{g}{\omega_{ci}} \hat{\mathbf{y}}, \tag{7}$$

$$\mathbf{v}_d = \frac{\hat{\mathbf{z}} \times \nabla p_i}{n e B_0} c, \tag{8}$$

and

$$\mathbf{v}_p = -\left[\frac{\partial}{\partial t} + (\mathbf{v}_E + \mathbf{v}_g) \cdot \nabla_\perp \right] \frac{\nabla_\perp (\phi_0 + \phi)}{\omega_{ci} B_0} c. \tag{9}$$

Here ϕ_0 is a background plasma potential. The ion equation of continuity and Eq. (5) imply

$$\left\{ \frac{\partial}{\partial t} + (\mathbf{v}_E + \mathbf{v}_g) \cdot \nabla_\perp \right\} n_i - \rho_s^2 \nabla_\perp \cdot \left\{ n_i \left[\frac{\partial}{\partial t} + (\mathbf{v}_E + \mathbf{v}_g) \cdot \nabla_\perp \right] \nabla_\perp \left(\tilde{\phi} + \tilde{\phi}_0 \right) \right\} = 0. \tag{10}$$

Setting $n_i = n_0(x) \left(1 + \tilde{n}_i\right)$, using $\tilde{\mathbf{v}}_E = \frac{\hat{\mathbf{z}} \times \nabla \tilde{\phi}}{B_0} c$ and defining

$$v_0 = \frac{c}{B_0} \frac{\partial \phi_0}{\partial x} + \frac{g}{\omega_{ci}}, \tag{11}$$

which is the ambient ion flow velocity, Eq. (10) yields

$$\left(\frac{\partial}{\partial t} + (\mathbf{v}_E + \mathbf{v}_g) \cdot \nabla_\perp \right) \left(\tilde{n}_i - \frac{1}{n_0} \rho_s^2 \nabla_\perp \cdot n_0 \nabla_\perp \tilde{\phi} \right) = -\rho_s^2 v_0'' \frac{\partial \tilde{\phi}}{\partial y} + \frac{c_s \rho_s}{L_n} \frac{\partial \tilde{\phi}}{\partial y} - \frac{\rho_s^2}{L_n} v_0' \frac{\partial \tilde{\phi}}{\partial y}, \tag{12}$$

where the prime indicates d/dx. Equations (4), (12) and the charge neutrality condition of Eq. (1) are our basic equations. Note that only the dominant nonlinearity is retained in Eq. (12), as in Eq. (4).

In the absence of the gravitational drift velocity and for a uniform $\mathbf{v}_E$ the coupled Eqs. (4) and (12) reduce to the well-known Hasegawa-Wakatani equations[17] describing the collisional drift wave. In the low collisionality-strong shear limit $k_\parallel^2 v_e^2 > \nu_e |\omega_k|$ the density is forced to

be close to the local Boltzmann distribution and the equations reduce to the single dissipative equation[18] often used to study driftwave turbulence. Including the gravitational acceleration g/L_n gives the resistive g mode for the collision dominated plasma and an additional stabilizing or destabilizing effect to the drift wave in the weak collisionality regime.

Let us look at a linearized wave equation for a mode which varies as $\exp\left(-i\omega t + iky + ik_{\parallel}(x)z\right)$ where $k_{\parallel}(x) = kx/L_s$. Eliminating $\tilde{n} = \tilde{n}_i = \tilde{n}_e$ from Eqs. (4) and (12), we obtain

$$\frac{1}{n_0}\rho_s^2 \frac{d}{dx} n_0 \left(\frac{d}{dx}\tilde{\phi}\right) = \left[\rho_s^2 k^2 - \frac{\rho_s^2 k\left(v_0'' + v_0'/L_n\right)}{\omega - kv_0} + \frac{kv_g + ik_{\parallel}^2 D_{\parallel}}{\left(\omega - kv_0\right)\left(\omega - kv_{E0} + ik_{\parallel}^2 D_{\parallel}\right)}\frac{k\rho_s c_s}{L_n}\right.$$

$$\left. + \frac{ik_{\parallel}^2 D_{\parallel}}{\omega - kv_{E0} + ik_{\parallel}^2 D_{\parallel}}\right]\tilde{\phi}, \tag{13}$$

where $D_{\parallel} = v_e^2/\nu_e$ is the parallel electron diffusion coefficient and $v_{E0} = c\partial\phi_0/B\partial x$.

We derive dispersion relations for the following two cases. Case 1) discontinuous density step: $b \to 0$, $n_0 = n_1$, for $x > 0$, $n_0 = n_2$ for $x < 0$ and $U/a = $ constant as $a \to \infty$. Case 2) smooth density change: $a = b$ and $n_0(x) = n_0 \exp\left(x/L_n\right)$ for $|x| < b$.

Case 1. Discontinuous density step.

Setting $v_0'' = 0$, a solution of Eq. (13) is written as follows:

$$\tilde{\phi} = Ae^{-kx}, \qquad x > 0,$$

and

$$\tilde{\phi} = De^{kx}, \qquad x < 0.$$

The jump conditions at $x = 0$ are

$$A = D \tag{14}$$

and

$$\rho_s^2 \left[n_1 \frac{d\tilde{\phi}}{dx}\bigg|_{x=+0} - n_2 \frac{d\tilde{\phi}}{dx}\bigg|_{x=-0}\right] = k\frac{(n_2 - n_1)v_0'\rho_s^2}{\omega}\tilde{\phi} + \frac{\rho_s k^2 v_g c_s (n_1 - n_2)}{\omega(\omega - kv_g)}\tilde{\phi}. \tag{15}$$

11

Using Eqs. (14) and (15), the dispersion relation is written as

$$\omega \left(\omega - k v_g \right) - \alpha \frac{u}{a} \left(\omega - k v_g \right) + \alpha k g = 0, \tag{16}$$

which yields

$$\omega = \frac{1}{2} \left(k v_g + \frac{\alpha u}{a} \right) \pm \frac{1}{2} \sqrt{\left(k v_g - \frac{\alpha u}{a} \right)^2 - 4 \alpha k g}, \tag{17}$$

where $\alpha = (n_1 - n_2) / (n_1 + n_2)$ is the Attwood number. The interchange mode is unstable when $2\sqrt{\alpha k g} \geq \left| \frac{\alpha u}{a} - k v_g \right|$. Hence, the interchange process is stabilized by the shear flow when

$$\sqrt{\alpha} \frac{u}{2a} \geq \sqrt{k g}. \tag{18}$$

Case 2. Smooth density change.

Here $a = b$ and $n_0(x) = n_0 \exp\left(x/L_n\right)$ for $|x| < a$ and $k_\parallel = k x / L_s$ as shown in Fig. 1. The eigenmode is

$$\tilde{\phi} = \begin{cases} A \exp\left[\int_a^x \kappa_1 dx\right], & \text{for} \quad x > a \\ B \exp\left[\int_a^x \kappa_1 dx\right] + C \exp\left[\int_{-a}^x \kappa_2 dx\right], & \text{for} \quad |x| < a \\ D \exp\left[\int_{-a}^x \kappa_2 dx\right], & \text{for} \quad x < 0, \end{cases} \tag{19}$$

where the WKB approximation has been used in writing Eq. (19). The validity of the approximation is discussed later. In Eq. (19), $\kappa_1 = -\frac{1}{2L_n} - q$, $\kappa_2 = -\frac{1}{2L_n} + q$

$$q(x) = \left[\frac{1}{4L^2} + k^2 - \frac{k v / L_n a}{\omega - k v_0} + \frac{(k v_g + i\nu) k c_s}{(\omega - k v_0)(\omega - k v_{E0} + i\nu) L_n \rho_s} + \frac{i\nu / \rho_s^2}{\omega - k v_{E0} + i\nu} \right]^{1/2}, \tag{20}$$

$\nu = k_\parallel^2 D_\parallel$ and we assume $\text{Re}\,\kappa_1 < 0$ and $\text{Re}\,\kappa_2 > 0$. The jump conditions are

$$\left. \begin{array}{l} A = B + C e^{\psi_2} \\ D = B e^{-\psi_1} + C \end{array} \right\} \tag{21}$$

and

$$\kappa_1'(a) A - \kappa_1(a) B - \kappa_2(a) C e^{\psi_2} = \frac{k u / a}{\omega - k u - k v_g} A$$

$$\kappa_1(-a) B e^{-\psi_1} + \kappa_2(-a) C - \kappa_2'(-a) D = -\frac{k u / a}{\omega + k u - k v_g} D. \tag{22}$$

Here $\psi_{1,2} = \int_{-a}^{a} \kappa_{1,2}(x)dx$. Equations (21) and (22) yield the dispersion relation

$$\left[\kappa_1'(a) - \kappa_1(a) - \frac{ku/a}{\omega - k(u + v_g)}\right]\left[\kappa_2(-a) - \kappa_2'(-a) + \frac{ku/a}{\omega + k(u - v_g)}\right]$$

$$- \left[\kappa_1'(a) - \kappa_2(a) - \frac{ku/a}{\omega - ku - ku_g}\right]\left[\kappa_1(-a) - \kappa_2'(-a) + \frac{ku/a}{\omega + ku - kv_g}\right]e^{-\psi_1+\psi_2}$$

$$= 0, \tag{23}$$

where $\kappa_1'(a) = \kappa_1(a)\big|_{1/L_n=0}$ and $\kappa_2'(-a) = \kappa_2(-a)\big|_{1/L_n=0}$. This dispersion relation includes both the K-H instability and the interchange or the resistive pressure-gradient driven instability.

[Case 2-a] First of all, we look at the magnetic shear stabilization of the K-H instability. The density gradient $1/L_n$ and v_g are set zero in Eq. (23) to obtain

$$\frac{(ku/a)^2}{\omega^2 - k^2u^2}\exp\left[-2\int_{-a}^{a} q_r dx\right] + \left(2q_+ + \frac{ku/a}{\omega - ku}\right)\left(2q_- - \frac{ku/a}{\omega + ku}\right) = 0, \tag{24}$$

where q_r and q_i are a real and imaginary part of q, respectively, and $q_\pm = q(\pm a)$. As for the growing mode, we assume $\omega = i\gamma$ is pure imaginary. This assumption is justified since the imaginary part of the left-hand side of Eq. (24) is proportional to the real part of ω which can be set zero. Equation (24) is rewritten by keeping in mind $q_+ = q_-^* \equiv q_r(a) + iq_i(a)$ as follows:

$$\gamma^2 - \frac{kuq_i(a)}{a|q_+|^2}\gamma + \frac{1}{4|q_+|^2}\left(\frac{ku}{a}\right)^2\left(1 - 4aq_r(a) - e^{-2\int_{-a}^{a} q_r dx} + 4a^2\left(q_r^2 + q_i^2\right)\right) = 0, \tag{25}$$

which yields

$$\gamma\frac{a}{u} = \frac{kq_i(a)}{|q_+|^2} \pm \frac{k}{2}\frac{1}{|q_+|^2}\left\{q_i^2(a) + |q_+|^2\left(e^{-2\int_{-a}^{a} q_r dx} - 4a^2|q_+|^2 + 4q_r a - 1\right)\right\}^{1/2}, \tag{26}$$

where

$$q_r(a) = \left[\left(s^2 + t^2\right)^{1/2} + s\right]^{1/2}\Big/\sqrt{2}, \tag{27}$$

$$q_i(a) = -\left[\left(s^2 + t^2\right)^{1/2} - s\right]^{1/2}\Big/\sqrt{2}, \tag{28}$$

13

and

$$s \;=\; k^2 + \frac{\nu(\nu+\gamma)/\rho_s^2}{(\nu+\gamma)^2 + k^2 u^2} \;\simeq\; k^2 + \frac{\nu^2/\rho_s^2}{\nu^2 + k^2 u^2}, \tag{29}$$

$$t \;=\; \frac{\nu k u/\rho_s^2}{(\nu+\gamma)^2 + k^2 u^2} \;\simeq\; \frac{\nu k u/\rho_s^2}{\nu^2 + k^2 u^2}. \tag{30}$$

Since $q_i(a)$ in Eq. (26) is negative, the K-H mode is unstable when

$$e^{-2\int_{-a}^{a} q_r dx} - (2q_r(a)a - 1)^2 - 4q_i^2(a)a^2 > 0. \tag{31}$$

Roughly speaking, the maximum growth rate is at $q_r(a)a \simeq ka \simeq 1/2$ and the threshold with respect to the parallel wavenumber is

$$ak_\parallel(a) < \frac{1}{2\sqrt{e}} \sqrt{\frac{u\rho_s^2}{v_e l_e a}}. \tag{32}$$

When the shear scale length L_s is shorter than

$$L_s = a\sqrt{e} \left(\frac{v_e l_e a}{u\rho_s^2}\right)^{1/2}, \tag{33}$$

all of the K-H mode will be stabilized. As we show later, when the magnetic field tilting angle $\theta = k_\parallel/k$ is greater than 0.02, the K-H modes is not seen to grow in the simulation. This angle is much greater than that of Eq. (32) for the present simulation parameters.

[**Case 2-b**] Without shear flow and magnetic shear, the dispersion relation (24) gives the growth rate of the interchange instability for a finite density gradient. Equation (23) reduces to

$$\tanh(2aq) = -\frac{2kq}{k^2 + q^2}, \tag{34}$$

where we assume $kL_n \approx L_n/\rho_s \gg 1$ and approximate

$$\kappa_{1,2} \;\equiv\; \pm q,$$

$$q \;=\; k\left(1 + \frac{g/L_n}{(\omega - ku_g)\omega}\right)^{1/2}. \tag{35}$$

Setting $q = iz$, Eq. (34) becomes

$$f(z) = \tan(2az) = \frac{2kz}{z^2 - k^2}.$$ (36)

Solutions of the dispersion relation correspond to the cross points of Fig. 2. As seen in Fig. 2, the solutions of $|z/k| < 1$ are approximately given by

$$za \simeq \frac{\pi}{2}l, \qquad l = \pm 1, \pm 2, \ldots$$ (37)

which yields the frequency

$$\omega = \frac{kv_g}{2} \pm \frac{i}{2} \sqrt{\frac{k^2 g/L_n}{k^2 + \pi^2 l^2/4a^2} - k^2 v_g^2}.$$ (38)

Therefore, the mode is unstable when

$$a^2 \omega_{ci}^2 / gL_n > k^2 a^2 + (\pi l/2)^2.$$

Since $g \simeq c_s^2/R$ for the magnetic field curvature R and $R \gtrsim L_n$, the mode is unstable up to $k \gtrsim 1/\rho_s$.

[**Case 2-c**] Finally, we briefly discuss the velocity shear effects on the interchange instability in a finite density gradient. By a process similar to the derivation of Eq. (36) from Eq. (23), we rewrite Eq. (23) without any approximation to obtain

$$\tan\left(-i \int_{-a}^{a} q(x)dx\right) = iT/S,$$ (39)

where

$$S = q_+ q_- + \left(\kappa_- + \frac{1}{2L_n}\right)\left(\kappa_+ - \frac{1}{2L_n}\right) - \frac{ku}{a}\frac{\kappa_+ - \frac{1}{2L_n}}{\omega - kv_g + ku}$$

$$+ \frac{ku}{a}\frac{\kappa_- - \frac{1}{2L_n}}{\omega - kv_g - ku} - \frac{k^2 u^2/a^2}{(\omega - kv_g)^2 - k^2 u^2},$$ (40)

$$T = \left(\frac{1}{2L_n} + \kappa_-\right)q_+ + \left(\kappa_+ - \frac{1}{2L_n}\right)q_- - \frac{ku}{a}\frac{q_+}{\omega - kv_g + ku} + \frac{ku}{a}\frac{q_-}{\omega - kv_g - ku},$$ (41)

$$\kappa_\pm = \left\{k^2 + i\nu/\rho_s^2 (\omega_\mp ku + i\nu)\right\}^{1/2},$$ (42)

$$\kappa_{1,2} = -\frac{1}{2L_n} \pm q,$$ (43)

and

$$q_\pm = q(\pm a). \qquad (44)$$

Since the dispersion relation of Eq. (39) is similar to Eq. (36), the solution of Eq. (39) is approximately given by

$$\int_{-a}^{a} q(x)dx = i\frac{\pi}{2}l + \delta, \qquad (l = 0, \pm 1, \pm 2, \dots) \qquad (45)$$

which corresponds to Eq. (37). The WKB approximation which was used to derive Eq. (19) is valid when the integer l is sufficiently large. Assuming $kL_n \gg 1$, $q(x)$ is approximated by

$$q(x) = \left[k^2 + \frac{(kv_g + i\nu)\,kc_s/L_n\rho_s}{(\omega - kv_0)(\omega - kv_{E0} + i\nu)} + \frac{i\nu/\rho_s^2}{\omega - kv_{E0} + i\nu} \right]^{1/2}. \qquad (46)$$

There are two resonances in Eq. (44), which are located at

$$x_{r1} = \frac{\omega - kv_g}{ku}a$$

and

$$x_{r2} = \frac{\omega + i\nu}{ku}a.$$

When $|\nu| \ll kv_g$, i.e., the magnetic shear is small enough, the distance between the two resonance points is av_g/ν. Evaluating $q(x)$ at the center of the two resonances, namely,

$$q\left(-v_g a/2u\right) \simeq k\left(1 - \frac{4g}{L_n}\frac{1}{k^2 v_g^2 - 4\omega^2}\right)^{1/2},$$

the growth rate obtained from Eq. (46) is roughly evaluated to be

$$\mathrm{Im}\,\omega = \frac{|k|v_g}{2}\sqrt{\frac{4ga^2/L_n u^2}{\frac{\pi^2}{4}l^2 + k^2 a^2 v_g^2/u^2} - 1}. \qquad (47)$$

Therefore, if

$$\sqrt{\frac{g}{L_n}}\frac{a}{u} < \frac{\pi}{4}l, \qquad (48)$$

the interchange mode is stabilized by the shear flow.

In unmagnetized plasmas the linearized equation, including equilibrium shear flow and gravity, is derived from the inviscid and incompressible fluid equations. The result is

$$\frac{1}{\rho_0}\frac{d}{dx}\left(\rho_0\frac{dv_x}{dx}\right) = \left\{k^2 + g\frac{k^2\rho_0'/\rho_0}{(\omega - kv_0)^2} + \frac{kv_0''}{\omega - kv_0} + \frac{kv_0'\rho_0'/\rho_0}{\omega - kv_0}\right\}v_x. \tag{49}$$

As for the shear flow stabilization of the Rayleigh-Taylor instability, the stabilization condition for the configuration of Case 1 is exactly the same as that given by Eq. (18). The criterion of Eq. (48) for Case 2 is also applicable to Eq. (49).

III.   Initial Value Simulation of Shear Flow Instabilities

The static uniform magnetic field B_0 is now in the z-direction only. The initial ion density is uniform $n_i = n_0$ in the x–y plane. The plasma is encased in a metallic box in the x-direction and periodic in the y-direction for most of the computer experiments we present, unless otherwise specified. We load the electrons with a density given by

$$n_e(x, t = 0) = n_0 + \frac{\Delta n_0}{\cosh^2(k_0 x)}, \tag{50}$$

where typically $\Delta n_0 = 0.1 n_0$ and $k_0 = 1/a$, with a being the shear layer width of the $E \times B$ flow produced by the charge separation $\rho_q = e(n_e(\infty) - n_0)$. The initial flow of the plasma produced by the charge or vorticity layer given in Eq. (50) is

$$v_y(x) = -\frac{4\pi n_0 e c}{k_0 B_0}\left(\frac{\Delta n_0}{n_0}\right)\tanh(k_0 x)$$

$$\equiv v_0 \tanh\left(\frac{x}{a}\right). \tag{51}$$

Although we vary parameters over a wide range, the typical set of parameters are as follows: the numbers of the grid points in the x- and y-directions $L_x = L_y = 64$, the numbers of particles in the x- and y-directions $N_x = N_y = 192$, the electron cyclotron frequency $\omega_{ce} = 80\omega_{pe}$ with ω_{pe} being the electron plasma frequency, the ion-to-electron mass ratio

17

$M/m = 1600$, the shear width $a = k_0^{-1} = 6\Delta$ with Δ being the unit grid separation, the electron and ion Debye lengths perpendicular to the external magnetic field direction $\lambda_{De} = \lambda_{Di} = 0$, the electron and ion Larmor radii $\rho_e = \rho_i = 0$, and the simulation time step $\Delta t = 200\omega_{pe}^{-1}$. (Note that the shear width is input as $a = 5$, which gives rise to the effective shear width of 6 due to the finite size particle effect.) The technique of loading electrons nonuniformly is different from the conventional technique. Instead of assigning a uniform weight of unity to an individual particle, the weight of the particle is determined by the fraction $n_e(x)/n_0$ dependent upon its initial location. The weight of the particle in the simulation is not changed throughout the run, although the code does allow for a change of weight as a function of time.[16] For example, the number of particles can be changed due to the creation (source) and the annihilation (sink) of particles; in a formulation of splitting "particles" into the background and perturbed distributions, the perturbed distribution can change their weight in time. In the reference simulations we choose $\Delta n_0/n_0 = 0.1$, the size of particles $a_x = a_y = 3\Delta$, and the decentering parameter[15] $\gamma_i = \gamma_e = 0.1$.

The linear theory[1,5,19] for the hyperbolic target profile of Eq. (51) gives that the Kelvin-Helmholtz mode is unstable for the wavenumbers k_y satisfying

$$k_y a < 1, \tag{52}$$

where $k_y = 2\pi m/L_y\Delta$ and m is the mode number in the y-direction. Figure 3 shows the electric potential $|\Phi|^2$ as a function of time for each mode ($m = 1 - 4$). Notice that because of the lack of noise in the implicit particle code, a large number of decades of exponential growth of the instability is observable. After a short period of time modes with $m = 1$ and 2 grow exponentially in time, while modes $m = 3$ and 4 do not grow until well into the nonlinear stage $t \sim 5 \times 10^4 \omega_{pe}^{-1} = 31a/v_0$. Here recall that the threshold mode number $m_c = L_y/a = 64/5$ and $m = 1, 2$ are supposed to be linearly unstable and $m \geq 3$ are stable. This is in agreement with simulation in Fig. 3. For these simulation parameters $\tilde{v} \equiv v_y (x = L_x) \Delta t/\Delta$ is equal to 0.75. The $m = 2$ mode shows a slight oscillatory feature

as seen near $t = 8 \times 10^4 \omega_{pe}^{-1} = 50a/v_0$. The modes with larger mode numbers are triggered unstable after the amplitude of the linearly unstable modes becomes high enough and the vortices of these modes begin to interfere or overlap around $t \sim 5 \times 10^4 \omega_{pe}^{-1}$.

Figure 4 exhibits a typical particle plot and the corresponding electrostatic potential contours. For clarity, only particles with initial velocity $v_y > 0$ on the left half at $t = 0$ are shown. Figure 4 is at $t = 1 \times 10^5 \omega_{pe}^{-1} = 62.5a/v_0$. In Fig. 5 we show the measured and theoretical growth rates of the modes. Figure 5 also shows the measured growth rate for the case when the magnetic field B_0 is tilted toward the y-direction from the z-direction by angle $\theta = 0.010$ radian. Note that this is less than the critical angle $(m_e/M_i)^{1/2} = 0.025$ radian. In this case the flow is still unstable although the magnitude of the growth rate is reduced by a factor of one order of magnitude and the unstable wavenumber increases, as is characteristic of drift wave-like modes. On the other hand, when we tilt the magnetic field away from the z-axis by $\theta = 3 \times 10^{-2}$, the system is stable. The electron thermal speed v_{th} is taken to be $0.05 \omega_{pe}\Delta$ in the tilted **B** field runs where electrons can move along the magnetic field line, while the thermal velocity perpendicular to **B** remains zero. Thus $k_\parallel v_{th} = 9.8 \times 10^{-4} m \omega_{pe}$ for the $\theta = 10^{-2}$ case, where m is the mode number in the y-direction. Thus $\gamma_{\max} < k_\parallel v_{th}$, where $\gamma_{\max} = 1.25 \times 10^{-4} \omega_{pe} = 0.20 v_0/a$ for the K-H mode (in Fig. 5). For $\theta = 3 \times 10^{-2}$, $k_\parallel v_{th} \gg \gamma^{K-H}$. The measured maximum growth rate for $\theta = 10^{-2}$ is $0.26 \times 10^{-4} \omega_{pe}$, about a fifth of the $\theta = 0$ case. When the normal mode is marginally stable, we find that the growth of the mode becomes secular as seen in Fig. 6. The electric potential due to the marginally unstable mode increases linearly with time.

As has been shown in the earlier driven simulations,[5] the stage at which the nonlinear triggering of other mode numbers sets in is coincident with the development of a vortex chain. In order to better control the study of the nonlinear problem of vortex evolution, our approach here is to separate the linear and nonlinear stages. We idealize the problem by starting from the secondary equilibrium of a vortex chain.

19

IV. Nonlinear Evolution of Vortices

In this section we initialize the simulation near the Stuart-Kelvin cat's eye equilibrium.[20,21] In the plasma context this amounts to the following initial electron density:

$$n_e(x, y) = n_0 + \frac{\Delta n_0 \left(1 - \epsilon^2\right)}{\left[\cosh\left(k_0 x\right) + \epsilon \cos\left(k_0 y\right)\right]^2}, \tag{53}$$

where $0 \leq \epsilon < 1$. The ion density is taken to be uniform $n_i = n_0$. The electrostatic potential resulting from these charge densities is

$$\phi(x, y) = \left(\frac{v_0}{k_0}\right) \ln\left(\cosh\left(k_0 x\right) + \epsilon \cos\left(k_0 y\right)\right). \tag{54}$$

Thus, the secondary equilibrium flow is given by

$$v_x = \frac{\epsilon v_0 \sin\left(k_0 y\right)}{\cosh\left(k_0 x\right) + \epsilon \cos\left(k_0 y\right)}$$

$$v_y = \frac{v_0 \sinh\left(k_0 x\right)}{\cosh\left(k_0 x\right) + \epsilon \cos\left(k y_0\right)}.$$

For $\epsilon = 0$, Eq. (53) reduces to Eq. (50). As ϵ is increased, the island structure of the equidensity contours becomes wider in the x-direction. We load electrons of nonuniform weight[16] to describe the nonuniform density distribution, and the parameters are the same as in Sec. III. With these parameters fixed, we vary ϵ from zero to the following set of values: 0.08, 0.3, 0.5, 0.6, 0.7, 0.85, and 0.95. The unit of frequency ω_{pe} is measured where $n_e = n_0$, $L_n/a = 64.5$, and the hydrodynamic unit of time a/v_0 at $x = 0$ or L_x is given by $a/v_0 \sim 1.6 \times 10^3 \omega_{pe}^{-1}$.

Figure 7 shows snapshots of particles with x, y coordinates and the corresponding electric potentials at various times for the case of $\epsilon = 0.08$. The instability is triggered by noise due to numerical truncation that results upon loading the particles, as there is no noise associated with the particle motion perpendicular to B with the initialization and the subsequent decentering algorithm.[15] At $t = 4.2 \times 10^4 \omega_{pe}^{-1} = 26 a/v_0$ the contour lines show a reconnection of the flow lines, reminiscent of the tearing instability of magnetic islands, that yields vortices

20

(islands) with smaller wavelengths ($m = 4$). Note the original vortices had mode number $m = 2$. At a later time the smaller induced islands ($m = 4$) are absorbed by the original islands ($m = 2$). In Fig. 7(c) and (f) at time $t = 6.6 \times 10^4 \omega_{pe}^{-1} = 41a/v_0$ we observe that the larger original vortices coalesce into one vortex with $m = 1$ in the direction of the exterior flow. We also see the vortex tilts in the clockwise sense due to the ambient external flow, which is downward on the right side of the vortex and upward on the left side.

During the coalescence process the perturbed electrostatic potential energy grows exponentially in time as shown in Fig. 8(a). Figure 8 summarizes the growth of the electrostatic energy for cases with various values of ϵ. The saturation of this energy in Fig. 8(a) happens shortly after a complete coalescence.

As we raise the value of ϵ and other parameters being fixed as before, the growth rate of the electrostatic energy increases as shown in Fig. 9. This figure will be further discussed in Sec. V. In frames (b)–(d) of Fig. 8 we also observe that a slight bump develops in the middle of the otherwise exponential growth phase. In particular Fig. 8(d) shows a faster than exponential growth in the early stage, while settling into a nearly exponential growth later. This indicates a transient growth that is faster than exponential growth for $\epsilon > \epsilon_{\text{crit}} \approx 0.5$. Another feature to be noticed in Fig. 8 is the amplitude oscillations after the coalescence. These are associated with the ringing of the vortex shape. This is reminiscent of the coalescence process of magnetic islands, although any parallelism of the coalescence of vortices in the present investigation with that of the magnetic island coalescence is perhaps fortuitous since the dynamical equations are rather different. Some conspicuous differences in the governing physics include: (i) the vortex dynamics is described by the single field ϕ, while the magnetic island dynamics requires at least two fields ϕ and the z-component of vector potential A_z; (ii) consequently there exists a magnetic repulsive force upon magnetic island coalescence, while in the vortex dynamics there is none; (iii) the magnetic flux conservation inhibits the reconnection of the magnetic flow lines. On the other hand the presence of the

21

Kelvin-Helmholtz instability and the coalescence instability for the vortex dynamics is similar to the presence of the tearing instability and the magnetic coalescence instability except for the frozen flux constraint that $d\psi/dt = \eta\nabla^2\psi \to 0$. The importance of the flux conservation constraint is easily seen in the formulas for the linear growth rates where $\gamma^{K\text{-}H} \sim k_y\Delta v_y$ but $\gamma^t \propto k_y^{2/3}\eta^{3/5}$.

In light of the above the actual dynamics of the tearing mode is in principle different from that for vortex coalescence dynamics. Ideas used to study the tearing, however, can be used to measure the vortex dynamics observed here. One measure is the vorticity difference between the original O-point and the innermost X-point (e.g., between A and B in Fig. 7 and Fig. 12), and another measure is the vorticity difference between the original O-point and the outermost X-point (e.g., between A and C in Fig. 7 and Fig. 12). The former measure of vorticity is indicated by circles and the latter measure by crosses in Fig. 10, for various ϵ cases. By definition of the former measure of vorticity vanishes when the two vortices complete their coalescence. See Fig. 10 and compare it with Fig. 8. On the other hand, the latter measure of vorticity may or may not vanish. In small ϵ runs [Figs. 10(a) and (b)] we see that it decreases until a certain point ($t \simeq 5 \times 10^4 \omega_{pe}^{-1} = 38.6a/v_0$) and then begins to increase. This manifests itself in a larger vortex at $t = 6.6 \times 10^4 \omega_{pe}^{-1} = 51a/v_0$ [e.g., Fig. 7(c)] than the original vortex. In larger ϵ experiments [Figs. 10(c) and (d)] the two measures depart, but both measures decrease, or at least not increase, even well after the coalescence.

Let us further examine the cases with $\epsilon = 0.3$ and $\epsilon = 0.6$, which are shown in Fig. 11 and Fig. 12, respectively. Figure 11(c) shows skewness of each vortex, as well as the tilt of the axis of two vortex centers measure in the negative direction. This is similar to the prediction by Horton et al.[1] and one found in the simulation.[5] More pronounced tilt may be seen in Fig. 12. The rotation of the axis continues even after the completion of the coalescence. We thus find that the chain of vortices is unstable against the tilt or rotational instability.

In Figs. 12(a)–(d) we observe the rotation of axis that connects the two O-points as they approach each other. Even after the coalescence the rotation continues. At the same time the overshooting oscillation (squashing of the droplet) continues. In this particular case, where $\epsilon = 0.6$, during the course of these droplet vibrations, fission of the vortex happens, as seen in Fig. 12(d). Observe in Fig. 12 that as the $m = 2$ vortices coalesce into an $m = 1$ vortex, much smaller scale vortices spring up. As the energy inversely cascades from the $m = 2$ vortices to the $m = 1$ vortex, the enstrophy cascades from $m = 2$ to higher m's, since both the overall enstrophy and energy are conserved. From the distribution of particles in plots in Figs. 7, 11, and 12, we note that even when the potential contours show fairly coherent patterns, the particles are strongly mixing in complex structures.

Figure 13 measures the negative of the rotational angle of the vortex-vortex axis as a function of time. As ϵ is increased, so is the growth of the angle. The rate of increase of the angle before $\theta = 180°$ is found to be faster than exponential. Following the terminology of magnetic coalescence this growth is called explosive growth. This explosive increase of θ saturates at or near $\theta = 180°$. In some cases θ stays around $180°$ after it reaches this position. In other cases after a brief pause at $\theta = 180°$ the angle again increases. The higher the value of θ, the stronger is this tendency for continued rotation. Figure 14 displays the distance between the two O-points as a function of time. Once again this distance $\delta r(t) = \sqrt{\Delta x^2 + \Delta y^2}$ also grows faster than exponential during the coalescence, indicating the explosive nature of the transients in the coalescence process. Note that different from θ in Fig. 13, the dependence of δr as a function of ϵ is not monotonically increasing. Also noted is that the increase of δr as a function of time is sometimes not monotonic.

Figure 15 shows the potential ϕ at $t = 0$ and a later time at which point a nearly $\pi/2$ rotation of the axis of a pair of vortices is realized for $\epsilon = 0.3$ and $\epsilon = 0.7$ cases. The evolution will be later compared with the theoretical model in Sec. V.

23

V. Localized Vortex Model

Now we present techniques for analytically modelling vortex simulation results, such as those presented in Secs. III and IV, by simple few degree-of-freedom Hamiltonian systems. This is a plausible goal as the system is nearly dissipationless and low wavenumber modes dominate the dynamics. The purpose here is two-fold: firstly, techniques are discussed in a manner that is quite general, more general than the present application. Secondly, the specific application of these techniques to the near cat's eye simulations are considered. The goal here being to elucidate the dynamical mechanism that are active during the coalescence or tilt instabilities.

The simulation results suggest that there is a large temporal regime where the two localized vortices of the initial condition remain isolated and maintain their *integrity* while moving. This suggests a few degree-of-freedom model for the flow, composed of localized interacting vortices, perhaps subject to an external field.

Since the computational studies of this paper are periodic in the y-direction, but not the x-direction, these boundary conditions must be incorporated into a model of the dynamics. The x boundary condition is straightforward, since to a large degree the motion of the localized vortices is far enough removed from the boundaries for us to assume $-\infty < x < \infty$. More generally one can satisfy finite metallic boundary conditions by appropriate configurations of image vortices. This is not pursued here for the x-direction, but the periodic y boundary condition does require images. These boundary conditions are perhaps a bit confusing since the simulations have a periodicity length of $4\pi/k_0$, while the initial conditions of interest are nearly $2\pi/k_0$ periodic. This latter near periodicity is not a constraint of the dynamics; thus unlike the $4\pi/k_0$ periodicity should not be built into the vortex model.

Begin by supposing that there are two vortices in the simulation domain, one denoted by "0" and the other by "1". Periodicity in the y-direction requires that each of these vortices be tracked by an infinite chain of equal strength vorticities. Vortices that track vortex 0 will

be denoted by an even subscript, while those that track vortex 1 by an odd subscript. The periodicity requirement thus demands the following constraints:

$$y_{2n}(t) = y_0(t) + \frac{4\pi n}{k_0}$$

$$y_{2n+1}(t) = y_1(t) + \frac{4\pi n}{k_0}$$

$$x_{2n}(t) = x_0(t)$$

$$x_{2n+1}(t) = x_1(t), \tag{55}$$

where $n = \pm 1, \pm 2, \pm 3, \ldots$.

In general suppose that the velocity at vortex n located at $\mathbf{x}_n \equiv (x_n, y_n)$, due to vortex m located at $\mathbf{x}_m$ is given by

$$\mathbf{v}_{nm} = \mathbf{V}(\mathbf{x}_n - \mathbf{x}_m). \tag{56}$$

Upon superposing, the total velocity at the location of vortex 0 is given by

$$\mathbf{v}_0 = \sum_{\substack{m=-\infty \\ m \neq 0}}^{\infty} \mathbf{V}(\mathbf{x}_0 - \mathbf{x}_m). \tag{57}$$

Similarly, for vortex 1

$$\mathbf{v}_1 = \sum_{\substack{m=-\infty \\ m \neq 1}}^{\infty} \mathbf{V}(\mathbf{x}_1 - \mathbf{x}_m). \tag{58}$$

Suppose that $\mathbf{V}$ is derivable from a stream function, defined by

$$\mathbf{V}(x, y) = \hat{z} \times \nabla \psi(x, y), \tag{59}$$

where ψ is even in both of its arguments

$$\psi(x, y) = \psi(-x, y) = \psi(x, -y). \tag{60}$$

Making use of these symmetry conditions and the periodicity constraints of Eq. (55) yields the following for Eqs. (57) and (58):

$$\mathbf{v}_0 = \sum_{m=-\infty}^{\infty} \hat{z} \times \nabla \psi \left(x_0 - x_1, y_0 - y_1 - \frac{4\pi m}{k_0} \right)$$

25

$$\mathbf{v}_1 = \sum_{m=-\infty}^{\infty} \hat{z} \times \nabla \psi \left(x_1 - x_0, y_1 - y_0 - \frac{4\pi m}{k_0} \right). \tag{61}$$

We ignore the self-interaction of the vortices and assume they move with the local flow. This yields the following Hamiltonian equations of motion:

$$\dot{x}_i = -\frac{\partial H}{\partial y_i} \qquad \dot{y}_i = \frac{\partial H}{\partial x_i} \qquad i = 0, 1, \tag{62}$$

where

$$H\left(x_0 - x_1, y_0 - y_1 \right) \equiv \sum_{m=-\infty}^{\infty} \psi \left(x_0 - x_1, y_0 - y_1 - \frac{4\pi m}{k_0} \right). \tag{63}$$

The form of the Hamiltonian of Eq. (63) suggests the introduction of the "center-of-mass" coordinates defined by

$$\xi = x_0 - x_1 \qquad \eta = y_0 - y_1$$

$$\mathcal{X} = x_1 + x_0 \qquad \mathcal{Y} = y_1 + y_0. \tag{64}$$

The coordinates $(\mathcal{X}, \mathcal{Y})$ remain fixed in time while (ξ, η) satisfy

$$\dot{\xi} = -\frac{\partial H}{\partial \eta}(\xi, \eta) \qquad \dot{\eta} = \frac{\partial H}{\partial \xi}(\xi, \eta). \tag{65}$$

In order to effect the modelling, it remains to determine the function $H(\xi, \eta)$. This can be achieved in two ways: first, a model H can be obtained directly by tracking the relative motion of the vortices. Since for this system physical space (ξ, η) is the phase space, and since trajectories lie on curves of constant H, one can attempt to fit H to the simulation output. Alternatively the vortex-vortex interaction ψ can be postulated, perhaps, by examination of the vortex shape. Knowing ψ, the sum of Eq. (63) must be evaluated in order to determine the dynamics.

Sometimes the sum of Eq. (63) can be evaluated in closed form; for example, in the case of point vortices where

$$\psi(\xi, \eta) = \psi_0 \ln \left(\xi^2 + \eta^2 \right), \tag{66}$$

26

this is the case. Defining $z = \frac{k_0}{4}(\eta + i\xi)$, it is evident that

$$J = \frac{\partial H}{\partial \eta} - i\frac{\partial H}{\partial \xi} = \frac{k_0\psi_0}{2} \sum_{m=-\infty}^{\infty} \frac{1}{z - m\pi}. \tag{67}$$

The sum of Eq. (67) is the Mittag-Leffler expansion for $\cot z$, which implies

$$J = \frac{k_0\psi_0}{2}\left[\frac{\sin\frac{k_0\eta}{2} - i\sinh\frac{k_0\xi}{2}}{\cosh\frac{k_0\xi}{2} - \cos\frac{k_0\eta}{2}}\right], \tag{68}$$

and thus from the first equality of (67) we obtain to, within an additive constant,

$$H(\xi,\eta) = \psi_0 \ln\left[\cosh\frac{k_0\xi}{2} - \cos\frac{k_0\eta}{2}\right]. \tag{69}$$

The summation performed above is related to the solved classical problem of obtaining the velocity field due to an infinite chain of point vortices,[22] but here the context is different in that H determines the dynamics subject to the constraints (55). H is not the stream function. Below we will construct the stream function as a function of time.

Now consider the inverse problem where H is assumed to be known and it is desired to construct ψ. The Poisson sum formula implies

$$
\begin{aligned}
H(\xi,\eta) &= \sum_{m=-\infty}^{\infty} \psi\left(\xi, \eta + \frac{4\pi m}{k_0}\right) \\
&= \sum_{m=-\infty}^{\infty} \tilde{\psi}(\xi, m)e^{im\frac{k_0\eta}{2}}, \tag{70}
\end{aligned}
$$

where ψ and $\tilde{\psi}$ are Fourier transform pairs, i.e.,

$$\tilde{\psi}(\xi, q) = \int_{-\infty}^{\infty} e^{iq\frac{k_0\eta}{2}}\psi(\xi,\eta)d\eta \tag{71}$$

$$\psi(\xi, \eta) = \frac{k_0}{4\pi}\int_{-\infty}^{\infty} e^{-iq\frac{k_0\eta}{2}}\tilde{\psi}(\xi, q)dq. \tag{72}$$

The function $\tilde{\psi}$ evaluated on integer values is determined by $H(\xi,\eta)$ according to

$$\tilde{\psi}(\xi, m) = \frac{k_0}{4\pi}\int_{-2\pi/k_0}^{2\pi/k_0} e^{-im\frac{k_0\eta}{2}}H(\xi,\eta)d\eta. \tag{73}$$

If one continues Eq. (73) for integer m to the entire real line, $\tilde{\psi}(\xi, q)$, $q \in \mathcal{R}$, then Eq. (72) can be used to obtain $\psi(\xi, \eta)$. Our goal of obtaining the vortex-vortex interaction potential is

27

then achieved. There is, however, a difficulty in this prescription because one must construct the continuation, which is not unique. A natural way to do this is to transform (73) to a contour integral around the unit circle in the complex plane. But, when m is not an integer a branch point occurs at the origin. A method of finishing the continuation involves the excising of a branch cut from the origin to infinity along the negative real axis of the complex plane and a deformation of the unit circle contour so as to skirt the cut. Further details of this method will not be presented here since for our specific purpose an artifice will be sufficient.

We propose the following form for H in the case where ε can differ from unity:

$$H(\xi, \eta; \varepsilon) = \psi_0 \ln \left[\sqrt{\frac{1}{2} (\varepsilon + \cosh k_0 \xi)} - \sqrt{\varepsilon} \cos \frac{k_0 \eta}{2} \right]. \tag{74}$$

Arguments in favor of this seemingly obscure choice will shortly be given, but first consider the inverse problem for obtaining $\psi(\xi, \eta; \varepsilon)$. Suppose ψ has the form of the point vortex interaction, except isotropy is broken by warping the x dependence of the interaction, i.e.,

$$\psi(\xi, \eta; \varepsilon) = \psi_0 \ln \left[f^2(\xi) + \eta^2 \right], \tag{75}$$

where the function $f(\xi)$ is yet to be determined. Substitution of f for ξ in our treatment of the point vortex case yields

$$\frac{\partial H}{\partial \eta} = \frac{k_0 \psi_0}{2} \frac{\sin \frac{k_0 \eta}{2}}{\cosh \frac{k_0 f}{2} - \cos \frac{k_0 \eta}{2}} \tag{76}$$

$$\frac{\partial H}{\partial f} = \frac{k_0 \psi_0}{2} \frac{\sinh \frac{k_0 f}{2}}{\cosh \frac{k_0 f}{2} - \cos \frac{k_0 \eta}{2}}. \tag{77}$$

Equations (76) and (77) imply

$$H(\xi, \eta; \varepsilon) = \psi_0 \ln \left[\cosh \frac{k_0 f}{2} - \cos \frac{k_0 \eta}{2} \right] + \text{const.} \tag{78}$$

Choosing the function f as follows:

$$\cosh (k_0 f) = \frac{1}{\varepsilon} \cosh (k_0 \xi) \tag{79}$$

28

results in, apart from an unimportant additive constant, the H given by Eq. (74).

There are several favorable attributes that lead one to choose the H of Eq. (74). To begin with, it is a continuous deformation away from the case where $\varepsilon = 1$, a case where the model exactly agrees with the simulation [c.f., Eq. (69)]. Thus at least near $\varepsilon = 1$ we expect reasonable agreement. Inspection of Eq. (79) reveals that for $\varepsilon \neq 1$ the logarithmic singularity at $\xi = \eta = 0$ has been eliminated. Any distributed vorticity arrangement will have this feature. Also, the anisotropy introduced is in agreement with that observed in the simulation (c.f., Fig. 16). In particular $\partial\psi/\partial\xi \big|_{\eta=0}$ dominates $\frac{\partial\psi}{\partial\eta}\big|_{\xi=0}$. A convincing argument in favor of the choice of Eq. (74) is that it leads to a $\phi(x,y,t)$ that as we shall see, looks like the simulation. We emphasize however that this choice is not unique and only qualitative agreement is sought.

The construction of $\phi(x,y,t)$ requires that the contributions from the double infinity of vortices be summed at each moment of time. We conclude that

$$\phi(x,y,t) = \sum_{m=-\infty}^{\infty} \left[\psi\left(x - x_0, y - y_0 - \frac{4\pi m}{k_0}\right) + \psi\left(x - x_1, y - y_1 - \frac{4\pi m}{k_0}\right) \right]. \qquad (80)$$

Without loss of generality the arbitrary constant can be dropped. Assuming

$$\mathcal{X} = \mathcal{Y} = 0$$

$$x_0 = \frac{1}{2}\xi \qquad x_1 = -\frac{1}{2}\xi$$

$$y_0 = \frac{1}{2}\eta \qquad y_1 = -\frac{1}{2}\eta, \qquad (81)$$

yields

$$\phi(x,y,t;\varepsilon) = H\left(x - \frac{\xi(t)}{2}, y - \frac{\eta(t)}{2}; \varepsilon\right) + H\left(x + \frac{\xi(t)}{2}, y + \frac{\eta(t)}{2}; \varepsilon\right). \qquad (82)$$

At time $t = 0$ Eq. (82) should represent the cat's eye initial condition. Using $\xi(t = 0) = 0$, $\eta(t = 0) = 2\pi/k_0$, Eq. (74) implies

$$\phi(x,y,0;\varepsilon) = \psi_0 \ln\left[\cosh k_0 x + \varepsilon \cos k_0 y\right], \qquad (83)$$

29

the equilibrium state desired. At later times

$$\phi(x,y,t;\varepsilon) = \psi_0 \ln \left\{ 2 \left(\sqrt{\frac{1}{2}\left[\varepsilon + \cosh k_0 \left(x - \frac{\xi(t)}{2}\right)\right]} - \sqrt{\varepsilon}\cos \frac{k_0}{2}\left(y - \frac{\eta(t)}{2}\right) \right) \right.$$

$$\left. \times \left(\sqrt{\frac{1}{2}\left[\varepsilon + \cosh k_0 \left(x + \frac{\xi(t)}{2}\right)\right]} - \sqrt{\varepsilon}\cos \frac{k_0}{2}\left(y + \frac{\eta(t)}{2}\right) \right) \right\}. \quad (84)$$

Now consider the comparison of the linear theory of the localized vortex model with the simulation. As noted above $\xi = 0$ and $\eta = 2\pi/k_0$ correspond to the cat's eye equilibrium, but also these correspond to dynamical equilibrium of the localized vortex model. This is evident upon differentiating Eq. (74). Moreover, expanding H to second order yields the following Hamiltonian for the linearized dynamics:

$$h(\delta\xi, \delta\eta; \varepsilon) = \frac{k_0^2 \psi_0 \sqrt{2}}{8\left(\sqrt{(1+\varepsilon)} + \sqrt{2\varepsilon}\right)} \left[-\sqrt{\varepsilon}\delta\eta^2 + \frac{\sqrt{2}\delta\xi^2}{\sqrt{1+\varepsilon}} \right]. \quad (85)$$

Thus the linear growth rate based on this model, normalized by $k_0^2\psi_0/4$, is given by

$$\hat{\gamma} = \frac{2^{3/4}\varepsilon^{1/4}}{(1+\varepsilon)^{1/4}\left(\sqrt{1+\varepsilon} + \sqrt{2\varepsilon}\right)}. \quad (86)$$

For $\varepsilon = 1$, $\hat{\gamma} = 1/2$, the classical result for the maximum growth rate of a row of point vortices. The localized vortex model selects the maximum because this is the only motion allowed by the periodicity constraints of Eqs. (55). Examination of Fig. 17 reveals that the simulation is in agreement in this limit. As $\varepsilon \to 0$, $\hat{\gamma} \sim 2^{3/4}\varepsilon^{1/4}$. This vanishing growth rate is in disagreement with the simulation, a not surprising result since the assumption of localization of the vortices breaks down. Because of $\varepsilon^{1/4}$ behavior this disagreement is confined to $0 \le \varepsilon \lesssim .2$. The theory is in reasonable agreement for a large range of ε away from unity. On Fig. 17 we have also plotted the results of Ref. 21, where the linear eigenvalue problem for the cat's eye equilibrium was solved numerically. Observe that for $\varepsilon \sim 0.3$ there appears to be a transition from localized vortex behavior to what we refer to as K-H behavior, i.e., sustainment of $\hat{\gamma}$. This is further evidenced in Fig. 10. On the other hand the theory

30

by Pierrehumbert and Windall is correct at $\epsilon = 0$ and agrees reasonably with simulation for $\epsilon < 0.3$ but unable to converge beyond.

Now consider the nonlinear behavior. Since H is conserved, one can obtain the orbits in physical space by simply plotting surfaces of constant H. In Fig. 18 we have done so for different values of ε. This figure shows that the energy surface decreases in width as ε decreases from 1 to zero. In the simulation it was observed that for small values of ε the instability that occurs is of the pairing or coalescence type, as shown in Fig. 10. For values of ε near unity the instability that occurs is of the tilt or rotational type. Figure 18 explains this tendency with ε. For all finite values of ε the vortices approach each other and move transverse to each other. For small ε the later motion decreases with the width of the energy surface and we observe the predominant coalescence.

In Fig. 19(b) we show the results of integrating Eqs. (65). $\theta(t)$ and $\delta r(t) = r(0) - r(t)$ for various values of ε are given. Many features of the corresponding quantities for the simulation Figs. 13 and 14 are reproduced as seen in Fig. 19(a). The initial conditions here were chosen near the separatrix, either just inside or just outside. In the case where the initial condition is just inside, θ can increase beyond 180°. This behavior is seen in Fig. 19(a) for the case where $\varepsilon = .95$ and in Fig. 19(b) for the case with $\varepsilon = ?$. When the initial condition is outside the separatrix, in the localized vortex model, θ can only approach 180°. This behavior is indicated in Fig. 19(a) by the flat spot near $\theta = 180°$ and shown in Fig. 19(b) for the case where $\varepsilon = ?$. Similarly Figs. 14 and 19 for $\delta r(t)$ show qualitative comparison.

Given the results of the orbit integration we can plot the stream function as a function of time by making use of Eq. (82). We have done so in Fig. 20(a) for the point vortex case where $\varepsilon = 1$ and $t = 0$, while Fig. 20(b) shows ϕ for $\varepsilon = 1$ and $t = \hat{t}$, a later time chosen so that $\theta \approx$. Similarly in Figs. 20(c) and 20(d) we plot ϕ for the case where $\varepsilon = .6$ and $t = 0$ and $t = \bar{t}$, respectively ($\bar{t}$ is chosen again so that $\theta \approx$). Figure 20 should be compared to Fig. 15.

In summary we see that there is qualitative agreement between the simulation and the localized vortex model with increasingly better agreement for larger ϵ.

VI.   Summary and Conclusions

We have derived linear theoretical stability conditions and growth rates for a plasma with shear flows taking into account gravity and magnetic shear. We analyze the stability problem with a discontinuous background density and with a smooth density. The dispersion relation shows the presence of $E \times B$ shear flows can stabilize the interchange and other related instabilities. The linear analysis of the gravitational instability shows that the interchange (R-T) mode is stabilized by the shear flow when the velocity shear $u/a \geq \sqrt{kg}$ or $\sqrt{g/L_n}$ (see Eqs. (18) and (48)). In the case of interchange mode, much shorter wavelength modes (much higher azimuthal modes) are destabilized. The mode is strongly localized near the mode rational surface. The interchange mode can be stabilized when $u/a \gtrsim (g/L_n)^{1/2}$. Nonlinear evolution of shear flow instability is on targeted special cases studied using the particle simulation method.

Implicit particle simulation results of the shear flow (K-H) instability due to $E \times B$ drift in a magnetized plasma show good agreement with the linear theory. The maximum growth $(0.2u/a)$ and the threshold wavenumber $(1/a)$ agree well with the observed growth rate and threshold. The linear K-H instability with $k_\parallel = 0$ has a sharp boundary between the stable and unstable wavenumbers, with the marginally stable modes having a local secular $(\sim t)$ growth arising perhaps from a ballistic resonance. In contrast, 3-D modes with $k_\parallel/k < \theta_c$ have a reduced growth rates. In the simulation, if the tilt angle $\theta \gtrsim 0.02$, the modes become rather drift wave-like and the growth rate is greatly reduced, while the unstable wavelength band expands. In the K-H instability, vortices that grow to a sufficient size trigger a secondary nonlinear instability with smaller, subharmonic wavenumbers.

The nonlinear instability is analyzed using a periodic chain of localized vortex structures,

using a periodic chain of localized vortex structure as an equilibrium (the Kelvin-Stuart cat's eye solutions). This equilibrium is observed to be unstable against the coalescence and tilt modes. The electrostatic energy increase of a lower wavenumber mode ($m = 1$) (the growth rate of $m = 1$ mode) is in reasonable agreement with the theory by Pierrehumbert and Windall[21] and the analysis of Sec. V. In a small amplitude regime, the tilt and coalescence instability and shear flow instability coexist. Even after the completion of coalescence, the shear flow instability continues. In the case of large amplitude, the tilt and coalescence instabilities dominate the shear flow instability. Upon overshoot of the tilt and coalescence, the coalesced vortices can again separate into two.

The growth rate of the tilt angle is in good agreement with the coalescence instability of a point vortices dynamic model in an appropriate range. The angle θ increases faster than the exponential function of time. The angle θ approaches π and stays for a long time. The point vortex model can accurately predict the time profile of the rotation angle of the vortices. The time scale prediction of the relative rotation of two vortices also provides a good explanation of the simulation.

The results for the stability of the transitional layer of a resistive plasma with a substantial change in density and perpendicular $E \times B$ flow velocity is given in terms of transcendental dispersion relation in Sec. II. The roots of the dispersion relations in the absence of shear flow describe the resistive g instability and the collisional drift wave instability with their different dependence on collisionality and magnetic shear. In the presence of a sheared flow the growth rates are strongly affected when the condition $k_y \Delta x u' > \gamma_k$ is satisfied where k_y, Δx, and γ_{k_y} are the parameters of the instability in the absence of the shear flow. The critical shear flow u' obtained from this condition is shown in Table I.

For the shear flows reported in TEXT tokamak plasma with the new higher resolution probe measurements the condition given above is marginally satisfied so that we conclude that shear flow may have an influence on the edge turbulence even if it is not sufficiently

33

strong to excite the K-H instability in that experiment.

There are two effects of the sheared $E \times B$ flow on the edge turbulence. Here, as in Ref. 1, we consider the direct effect of the shear flow on the wave dispersion relation showing that the growth rate of the mode present in the absence of shear flow can be strongly reduced. The second aspect is that even for a given fixed level of background waves the transport across the magnetic field is reduced by the shear flow. This decorrelation effect of the transport has been calculated by Shaing and Crume[9] and Biglari et al.[10] using the ideas of relative diffusion or clump turbulence theory. A simpler estimate of the reduction of the transport comes from considering the single particle motion of test particles in a dominant fluctuation of mode number k and strength $\tilde{\phi}_k$ the radial excursion size is reduced from the distance π/k_x between nodes of the radial modes to the size $\Delta r = \left(c\tilde{\phi}_k/Bu'\right)^{1/2}$ given by the strength of the shear flow u' and the amplitude of the potential fluctuation. Taylor et al.,[8] Shaing and Crume,[9] Biglari et al.,[10] and Taylor et al. and Burrell et al.[7] argue that the reduction in the plasma transport associated with L to H mode transition occurs either (1) due to the increased strength of the radial electric field or (2) due to the increased sheared flow velocity due to the deepening of the negative electrostatic potential well of the toroidal system. We show here that the increased strength of the shear flow changes the stability conditions of the plasma.

Sufficiently strong shear flow drives the plasma unstable to the K-H instability. We consider the unstable sheared flow regime with implicit particle simulations and describe the resulting vortex dynamics by the motions of the vortex cores. To make an analytic treatment of the vortex core dynamics, we idealize to the case of point vortex dynamics including the vortex-vortex interactions and the vortex-shear flow dynamics. The appears to give a good description of the principle processes of mutual rotations and coalescence of the vortices. Comparison with the simulations shows that a lowest order description of the turbulence follows by the vortex core dynamics and perhaps treating the density and pressure fields

as passively convected. The possibility of describing the relationship of the density and potential fluctuations measured in TEXT with the density being passively convected in the $E \times B$ flows given by the potential fluctuations has been previously suggested by Bengtson and Rhodes.[23]

Previous attempts to explain edge turbulence in TEXT by resistive hydrodynamic modes and by collisional modes have not been completely successful. The theoretical formulas used have neglected the effects of shear flow assuming that the background velocity simply Doppler shifted the frequencies of these instabilities. In view of the present theory and new measurements of Ritz et al.[24] reporting $dv_\theta/dr \leq 10^6$/sec a re-examination of the comparison between fluctuation theory and experiment may be necessary taking into account the finite value of dv_θ/dr.

The theory developed here may be relevant to the present ideas of the mechanisms operating in the L to H confinement mode transition as envisioned by the Shaing theory[2,9] which explains the transition as a change in the radial electric field due to bifurcation in the torque balance equation resulting from the nonlinear form of the radial ion current losses.

Acknowledgments

References

1. J. Liu, W. Horton, and J. E. Sedlak, Phys. Fluids **30**, 467 (1987) and W. Horton and J. Liu, Phys. Fluids **27**, 2067 (1984).

2. K. C. Shaing, "Effect of shear flow on resistive g turbulence" ORNL/P-89/2487 (1989) and Physics of Fluids, special issue (1990).

3. H. Takabe, L. Montierth, and R. L. Morse, Phys. Fluids **26**, 2299 (1983).

4. H. Takabe, K. Mima, L. Montierth, and R. L. Morse, Phys. Fluids **28**, 3676 (1985).

5. W. Horton, T. Tajima, and T. Kamimura, Phys. Fluids **30**, 3485 (1987).

6. R. J. Groebner, P. Gohil, K. H. Burrell, T. H. Osborne, R. P. Seraydarian, and H. St. John, in Proceedings of the 16th European Conference on Controlled Fusion and Plasma Physics, Budapest, Hungary, (European Physical Soc. 1989) Vol. I, p. 245.

7. K. H. Burrell et al., "Physics of the L to H Transition in the DIII-D Tokamak" to be published in Physics of Fluids edition of invited talks from Anaheim APS Meeting (1989).

8. R. J. Taylor, M. L. Brown, B. D. Fried, H. Grote, J. R. Liberati, G. J. Morales, P. Pribyl, D. Darrow, and M. Ono, Phys. Rev. Lett. **63**, 2365 (1989) and "Transport Modification by Radial Currents and the E-fields in Tokamaks" to be published in Physics of Fluids edition of invited talks from Anaheim APS Meeting (1989).

9. K. C. Shaing and E. C. Crume, Jr., Phys. Rev. Lett. **63**, 2369 (1989).

10. H. Biglari, P. H. Diamond, and P. W. Terry, Physics of Fluids B**2**, 1 (1990).

11. Theilhaber and C. K. Birdsall, Phys. Rev. Lett. **62**, 772 (1989).

12. J. S. Wagner, R. D. Sydora, T. Tajima, T. Hallinan, L. C. Lee, and S. I. Akasofu, J. Geophys. Res. **88**, 8013 (1983).

13. J. L. Burch, Rev. Space Sci. Space Phys. **21**, 463 (1983).

14. T. Tajima and J. N. Leboeuf, Phys. Fluids **23**, 884 (1980).

15. D. C. Barnes, T. Kamimura, J. N. Leboeuf, and T. Tajima, J. Comput. Phys. **52**, 480 (1983).

16. T. Tajima, **Computational Plasma Physics** (Addison-Wesley, Redwood City, 1989).

17. A. Hasegawa and M. Wakatani, Phys. Rev. Lett. **50**, 682 (1983) and M. Wakatani and A. Hasegawa, Phys. Fluids **27**, 611 (1984).

18. P. W. Terry and W. Horton, Phys. Fluids **25**, 491 (1982) and **26**, 106 (1983).

19. P. G. Drazin and L. N. Howard, J. Fluid Mech. **14**, 257 (1962).

20. J. T. Stuart, J. Fluid Mech. **29**, 417 (1967).

21. R. T. Pierrehumbert and S. E. Windall, J. Fluid Mech. **114**, 59 (1982).

22. H. Lamb, **Hydrodynamics**, Dover, 1945, Sixth Edition, New York, p. 225.

23. R. Bengtson and T. Rhodes (1989) private communication.

24. Ch. P. Ritz et al. (1989) private communication.

Table I. Effect of Shear Flow on Other Instabilities

Mode	Characteristics		Shear Flow Condition
	$k_y\Delta x$	γ_{k_y}	$k_y\Delta x u' > \gamma_r$
Rayleigh-Taylor	1	$\gamma_0 = \left(\dfrac{g}{L_n}\right)^{1/2}$	$u' > \left(\dfrac{g}{L_n}\right)^{1/2}$
Resistive-g	$\left(\dfrac{c^2\eta k_y^2}{4\pi\gamma_k}\right)^{1/2}$	$\gamma_{k_y} = \left(\dfrac{c^2\eta k_y^2}{4\pi}\right)^{1/3}\gamma_0^{2/3} > |\omega_*|$	$u' > \left(\dfrac{g}{L_n}\right)^{1/2}$
Eta-i $\eta_i = \dfrac{d\ln T}{d\ln n}$; η_c (threshold)	$k_y\rho_s\left(\dfrac{L_s}{r_n}\right)^{1/2}$	$\|\omega_*\|\dfrac{r_n}{L_s}(\eta_i - \eta_c)$; $k_y\rho_s \ll K_i^{-1/2}$ $\|\omega_*\|\left[\dfrac{r_n}{L_s}(\eta_i - \eta_c)\right]^{1/2}$; $k_y\rho_s \simeq K_i^{-1/2}$	$u' > \dfrac{c_s}{L_s}\left(\dfrac{r_n}{L_s}\right)^{1/2}(\eta_i - \eta_c)$ $u' > \dfrac{c_s}{L_s}(\eta_i - \eta_c)^{1/2}$
Collisional Drift Wave $k_\parallel^2 v_e^2 \sim \omega_*\nu_e$ $\quad l_e = \dfrac{v_e}{\nu_e}$	$\left(\dfrac{L_s^2}{l_e r_n}\right)^{1/2}\left(\dfrac{m_e}{m_i}\right)^{1/4}$	$\gamma_k \lesssim \|\omega_{*e}\| \lesssim \dfrac{c_s}{r_n}$	$u' > \dfrac{c_s}{(r_n L_s)^{1/2}}\left(\dfrac{l_e}{L_s}\right)^{1/2}\left(\dfrac{m_i}{m_e}\right)^{1/4}$
Dissipative Trapped Electron Mode $\varepsilon = \dfrac{r}{R}$	$k_y\rho_s\left(\dfrac{L_s}{r_n}\right)^{1/2}$	$\gamma_k \simeq \dfrac{\varepsilon^{3/2}\omega_*^2\eta_e}{\nu_e} \leq \|\omega_{*e}\|$	$u' > \left(\dfrac{r}{R}\right)^{3/2}\left(\dfrac{r_n}{L_s}\right)^{1/2}\dfrac{c_s^2}{\nu_e L_n L_{Te}}$

Figure Captions

1. (a) Slab geometry showing coordinates used to describe the sheared magnetic field $\mathbf{B}(x)$ and sheared flow velocity $v_y(x)$ along with the directions of ∇n_0 and g.

   (b) The piece-wise continuous profiles of the sheared flow velocity $v_y(x)$ and the density $n_0(x)$.

2. Graphical location of roots of the eigenvalue problem given by intersection of $F(z) = \tan(2az)$ and the right side of Eq. (37).

3. Evolution of the electric potential $\Phi_m^2(t)$ for modes $m = 1, 2, 3, 4$ for the reference parameters in Sec. III.

4. (a) Contour plot of the electrostatic potential at the critical time shown in part (b).

   (b) Position of particles in x–y plane with initial fluid velocities $v_y < 0$ at a critical stage of dynamics just before wave breaking.

5. Comparison of the measured growth rates with theoretical growth rate for the collisionless piece-wise linear slab flow. For the * data the tilt angle θ of the magnetic field is zero and for the $\triangle$ data the tilt angle is $\theta = 0.010$ radians.

6. Secular growth of the potential with a linear increase in time for a marginally stable mode.

7. (a)–(c) Contours of the electrostatic potential for the period doubling coalescence from the $m = 2$, $\epsilon = 0.08$ island chain.

   (d)–(f) Particles starting with $v_y < 0$ at later stages of the coalescence instability evolving from the period island chain of strength $\epsilon = 0.08$.

8. Evolution of the electrostatic potential energy from the nonlinear island chain as a function of increasing vortex strength ϵ.

9. Plot of normalized linear growth rate $\hat{\gamma}$ versus ε: $\times$ represents a data point extracted from the simulation results, $\otimes$ is a data point where it is difficult to ascertain the growth rate because the growth is faster than exponential; the dashed curve is the linear theory of Ref. 21; the solid curve is that derived form the localized vortex model.

10. Measure of the vorticity in the trapped coherent structures. The vorticity difference between the original O-point to the innermost X-point is given by the circles o and vorticity difference between the original O-point and the outermost X-point is given by the crosses $\times$.

11. Potential contours (a)–(c) and particle plots (d)–(f) for the period doubling coalescence of the $m = 2$, $\epsilon = 0.30$ island chain. Skewness of each vortex as the axis between two vortex centers rotates during coalescence.

12. As in Fig. 11 but a case of $\epsilon = 0.6$ with stronger tilting where the rotation continues after coalescence.

13. Simulation measurements for the rotation angle as a function of time $\theta(t)$ for labelled values of ε.

14. Distance between two O-points as a function of time $\delta r(t)$ as measured in the simulation for the labelled values of ϵ.

15. Equipotential contours obtained from the simulation: (a) $\varepsilon = .95$, $t = 0$; (b) $\varepsilon = .95$ at a later time; (c) $\varepsilon = 0.7$, $t = 0$; (d) $\varepsilon = 0.7$ at a later time.

16. Contours of the vortex-vortex interaction potential ψ given by Eqs. (75) and (79), for the cases (a) $\varepsilon = .05$, (b) $\varepsilon = .30$, (c) $\varepsilon = .70$, and (d) $\varepsilon = 1.0$.

17. Contours of constant interaction Hamiltonian, H, for (a) $\varepsilon = .05$, (b) $\varepsilon = .30$, (c) $\varepsilon = .70$, and (d) $\varepsilon = 1.0$.

18. Nonlinear results of localized vortex model. (a) $\theta(t)$ for $\varepsilon = .05, .30, .70$, and 1.0. (b) $\delta r(t)$ for the same ε values. (c) Plots of $\theta(t)$ that show trajectories with initial conditions on the two sides of the separatrix. (d) $\delta r(t)$ for two initial conditions. One just inside the other just outside the separatrix.

19. The stream function for the cases: (a) $\phi(x, y, 0; 1)$, (b) $\phi\left(x, y, \hat{t}; 1\right)$, (c) $\phi(x, y, 0; 0.6)$, and (d) $\phi\left(x, y, \bar{t}; 0.6\right)$. $\hat{t}$ and $\bar{t}$ are chosen so that the rotation is approximately $180°$.

(a)

(b)

FIG. 1

FIG. 2

FIG. 3

(a)

(b)

FIG. 4

growth rate $\left(\dfrac{\gamma a}{v_o}\right)$ ⟶

$k_y a$ ⟶

FIG. 5

FIG. 6

$\epsilon = 0.08$

(a)

(d)

$t\omega_p = 0$

(b)

C
A
B

(e)

$t\omega_p = 4.2 \times 10^4$

(c)

(f)

$t\omega_p = 6.6 \times 10^4$

FIG. 7

FIG. 8

FIG. 9

FIG. 10

$\epsilon = 0.08$

(a)

(d)

$t\omega_p = 0$

(b)

C
A
B

(e)

$\llcorner \; t\omega_p = 4.2 \times 10^4 \; \lrcorner$

(c)

(f)

$t\omega_p = 6.6 \times 10^4$

FIG. 11

$\epsilon = 0.60$
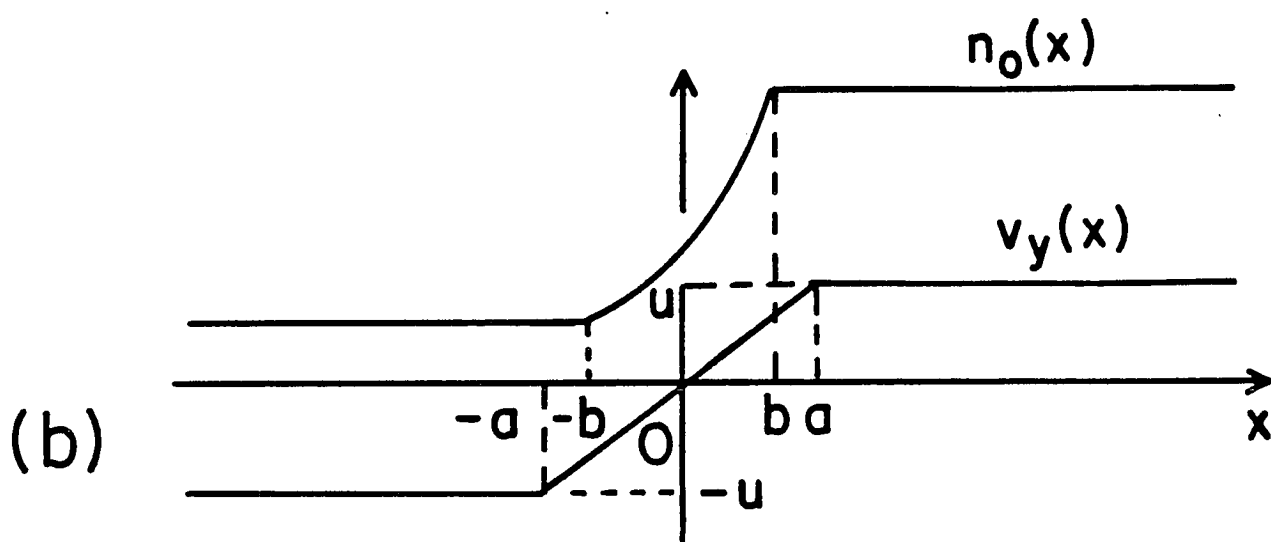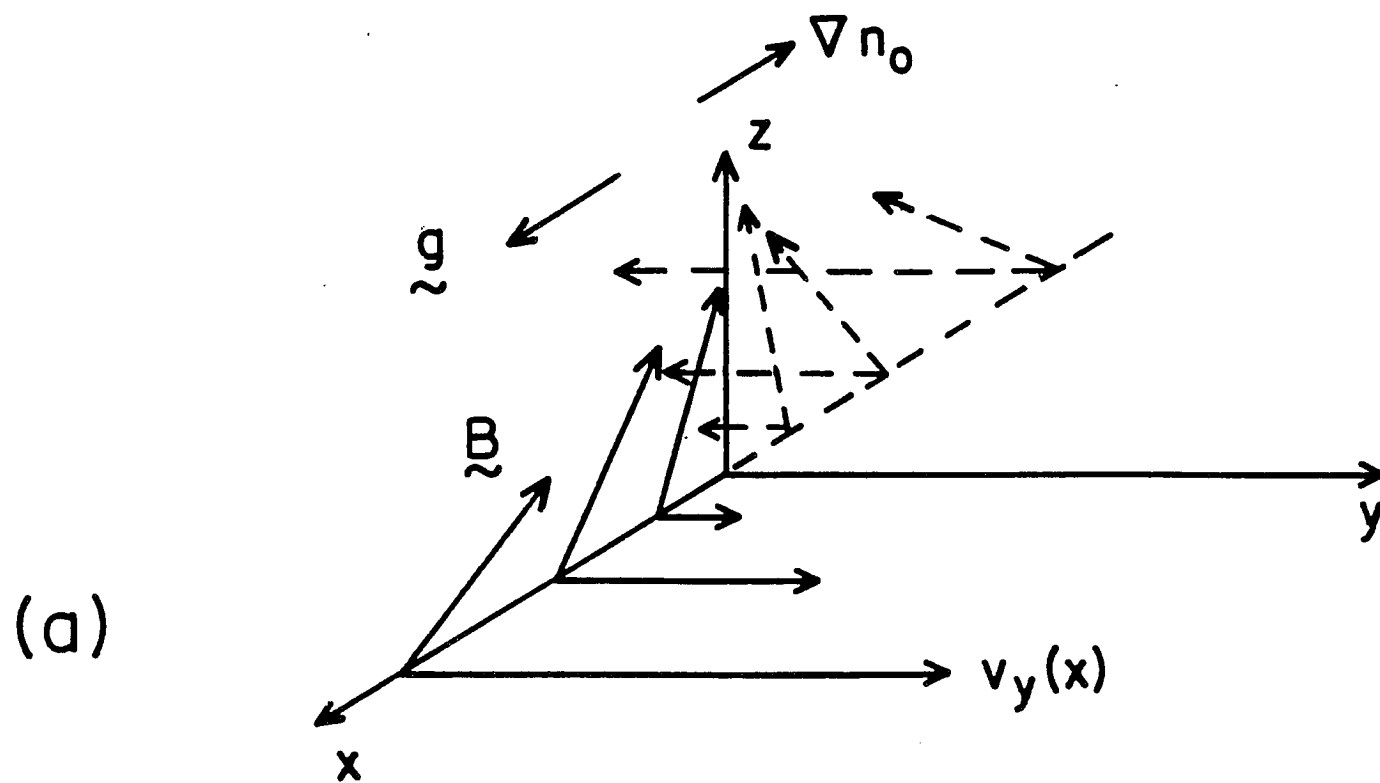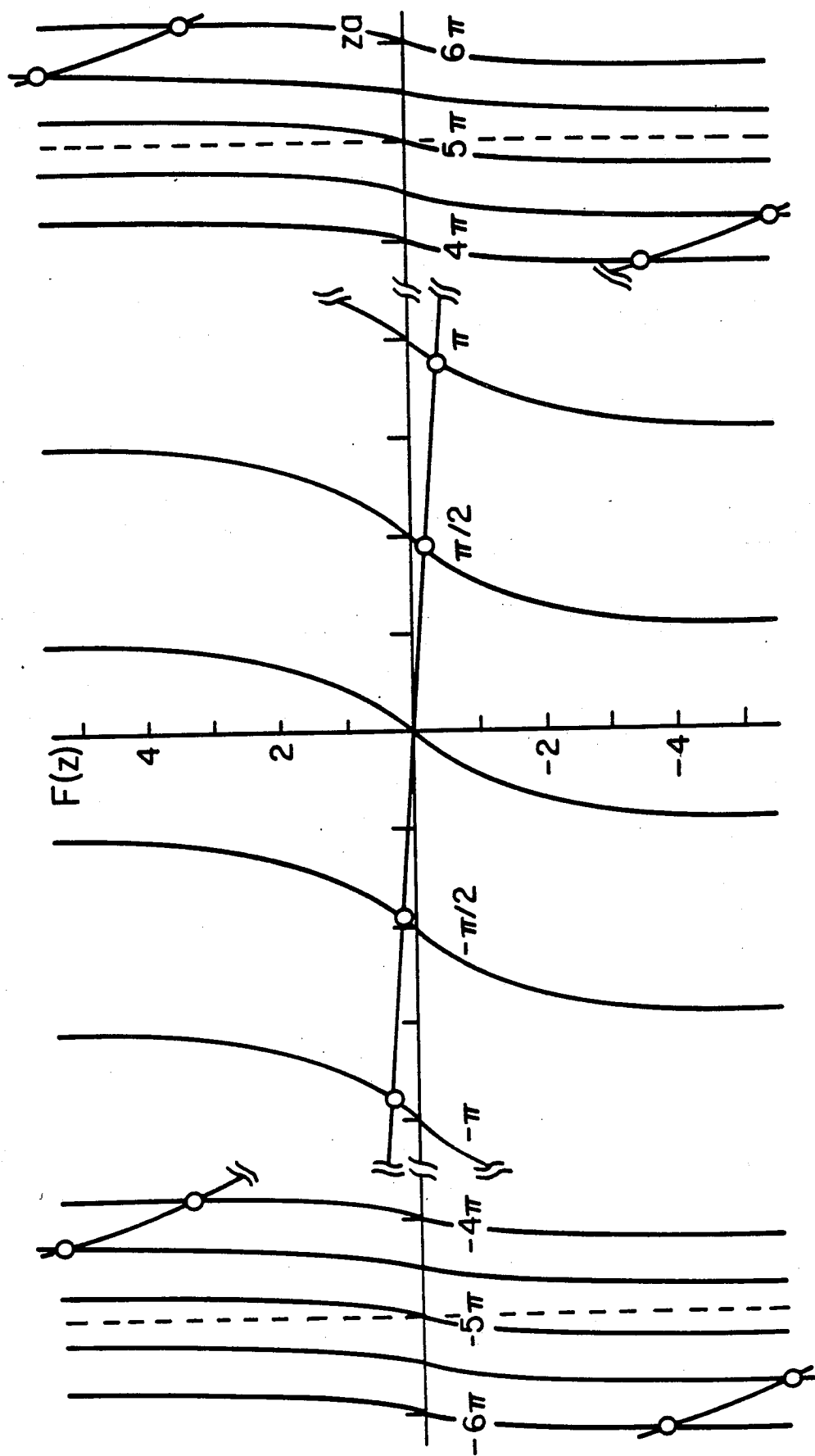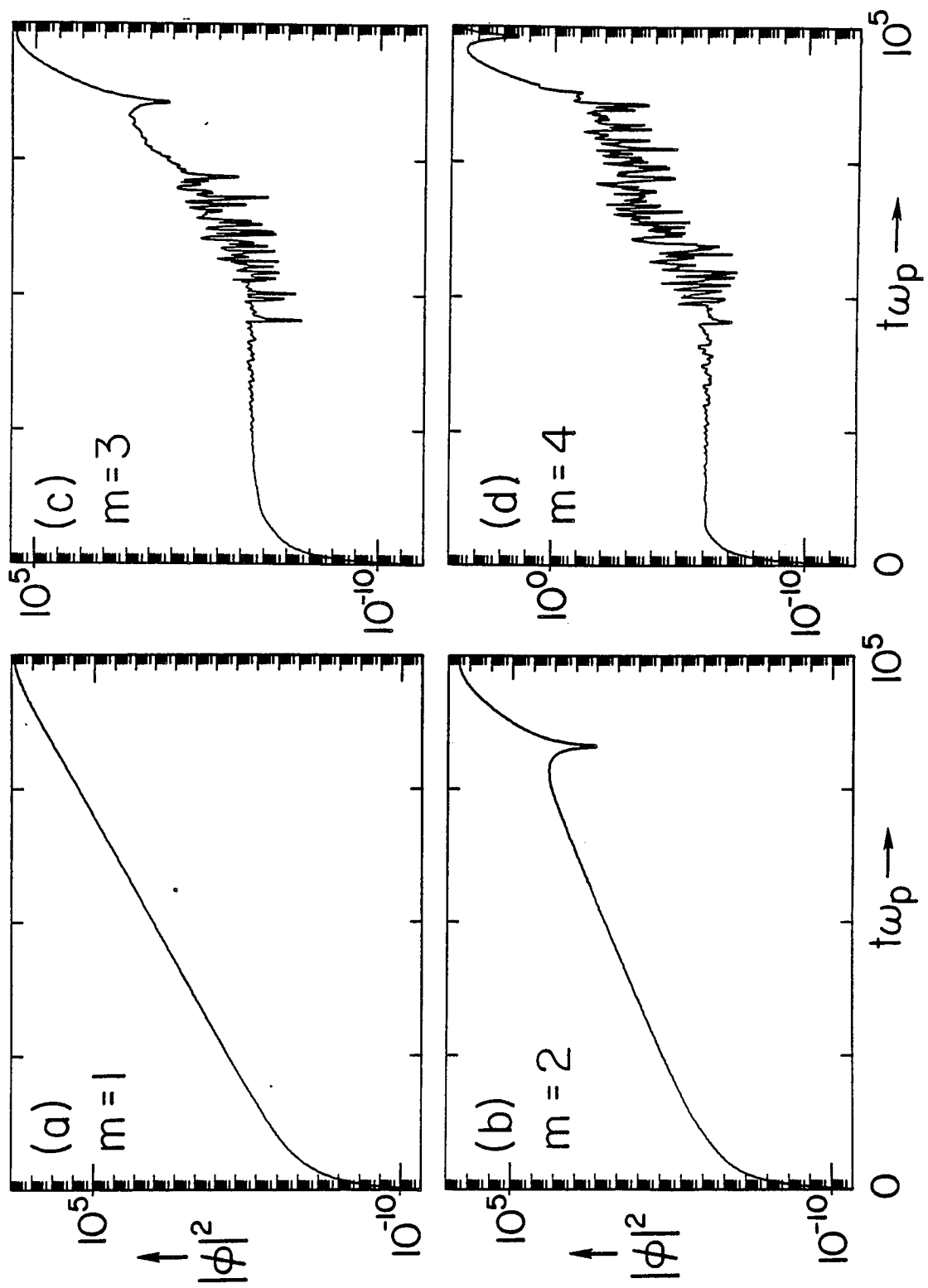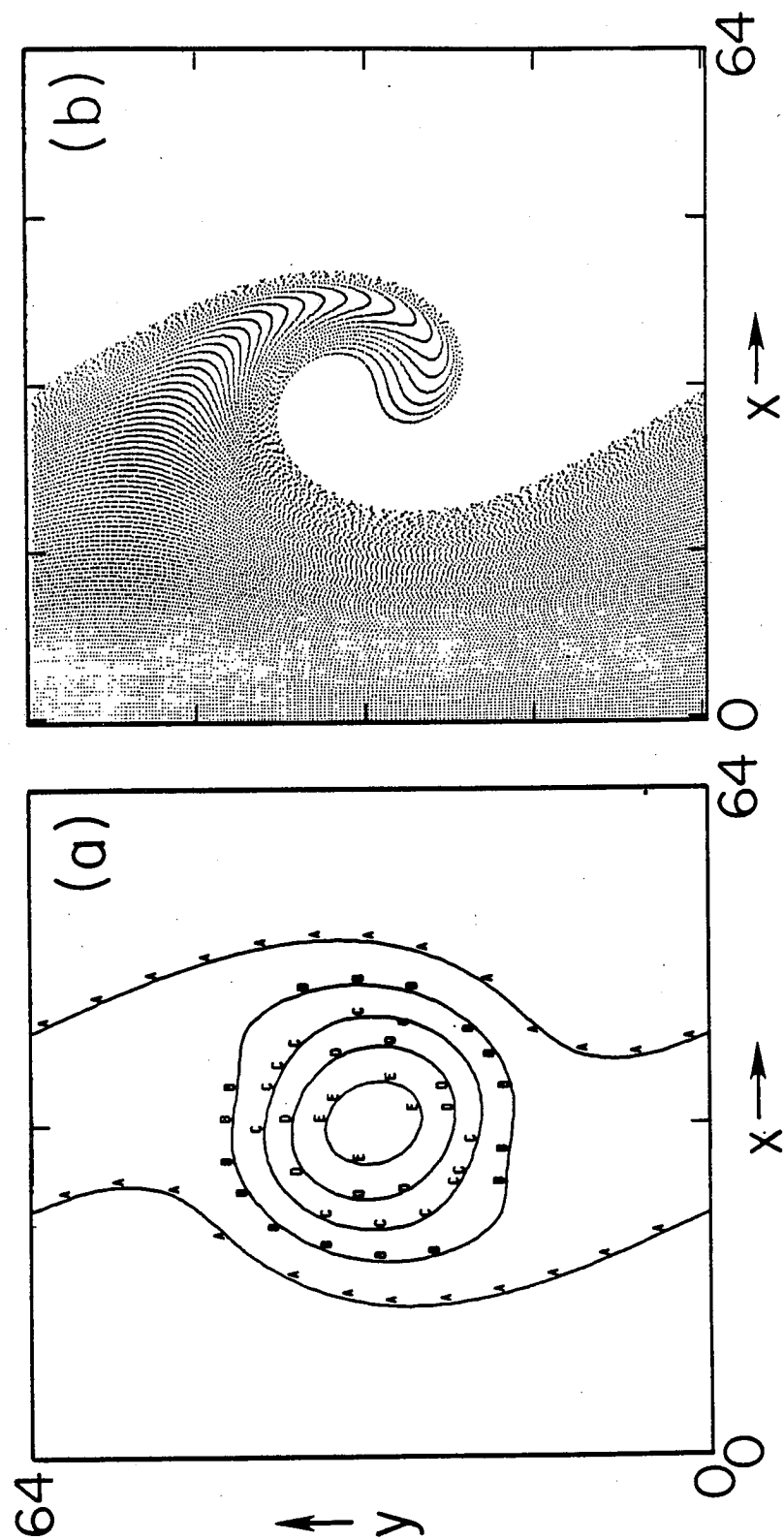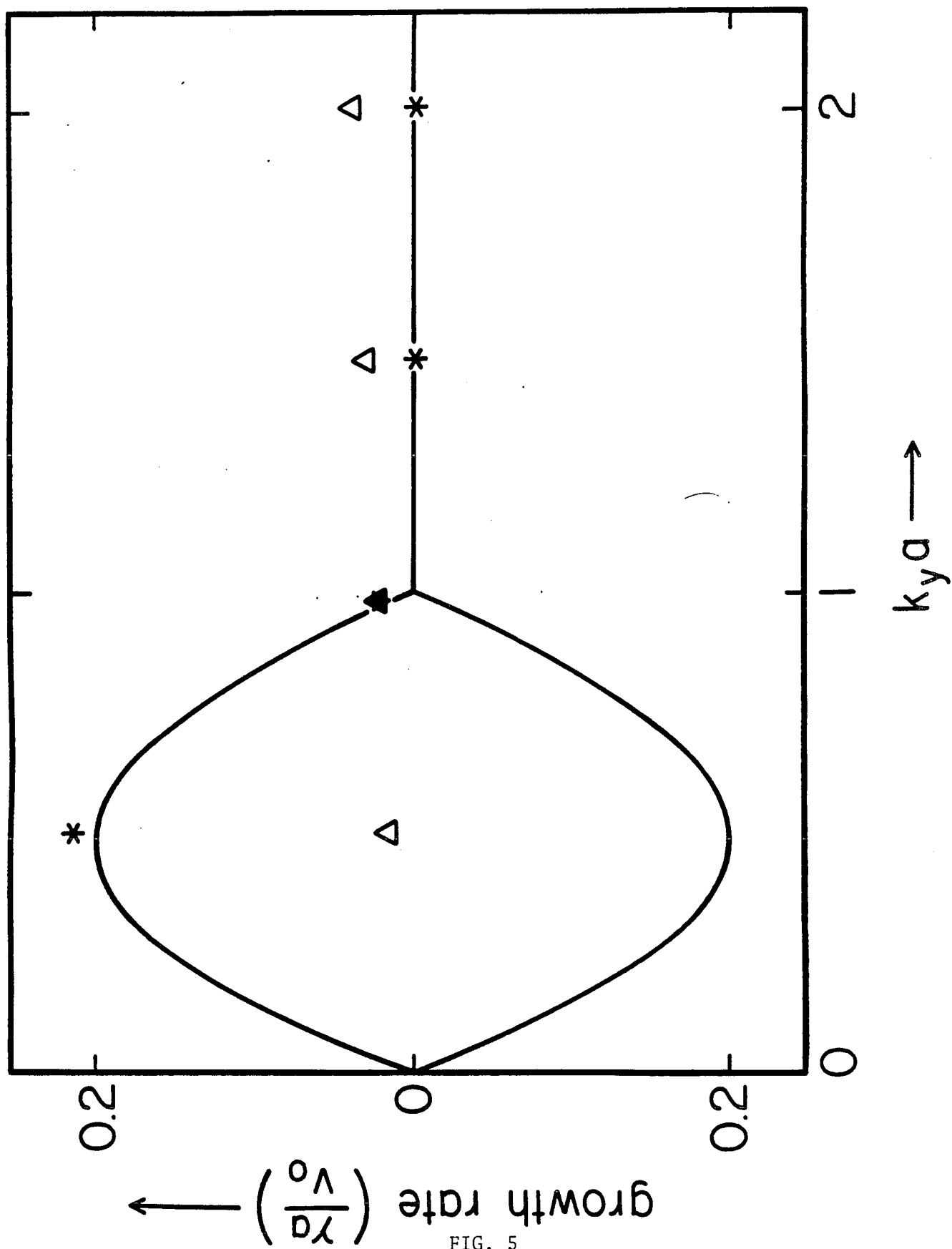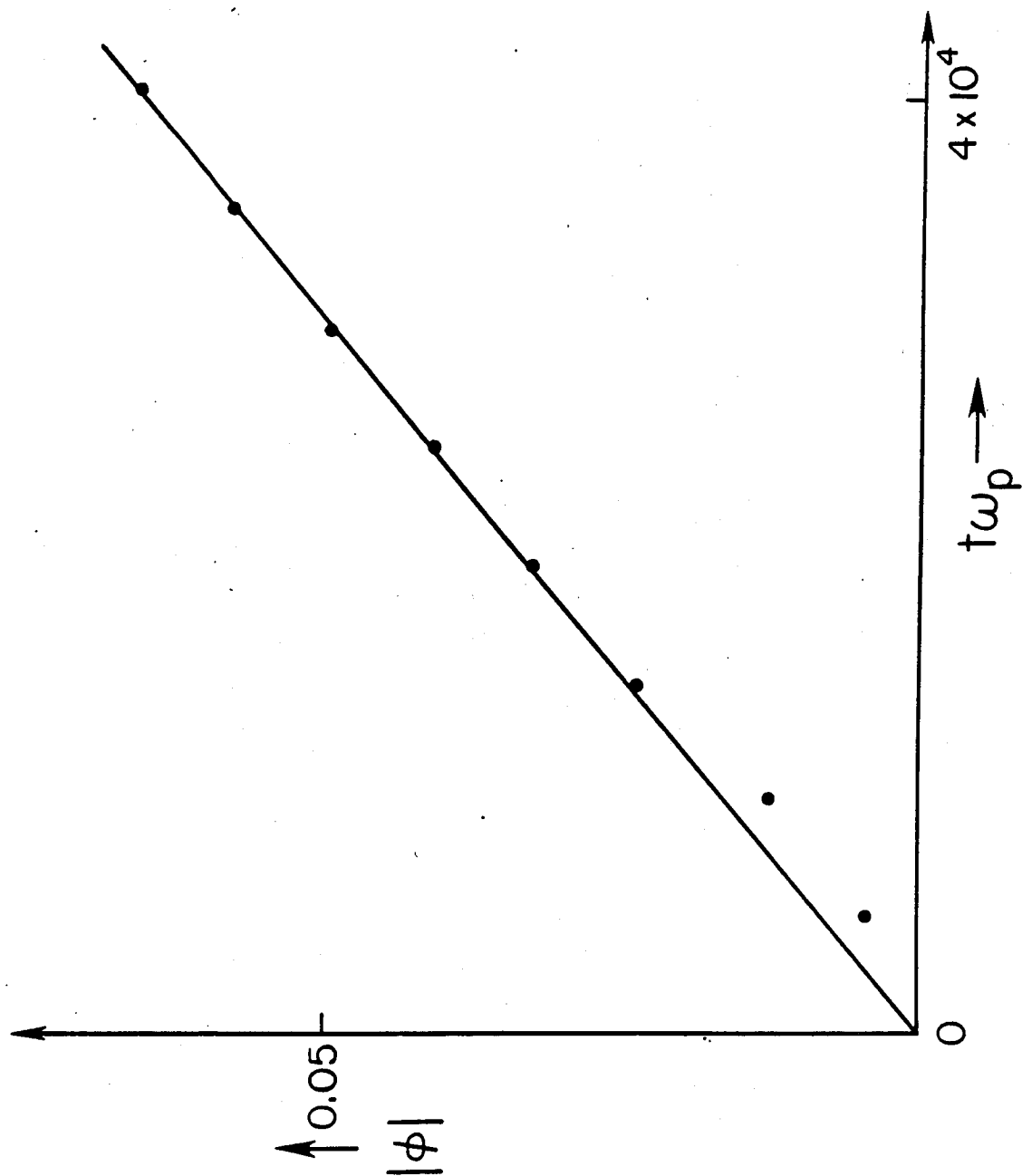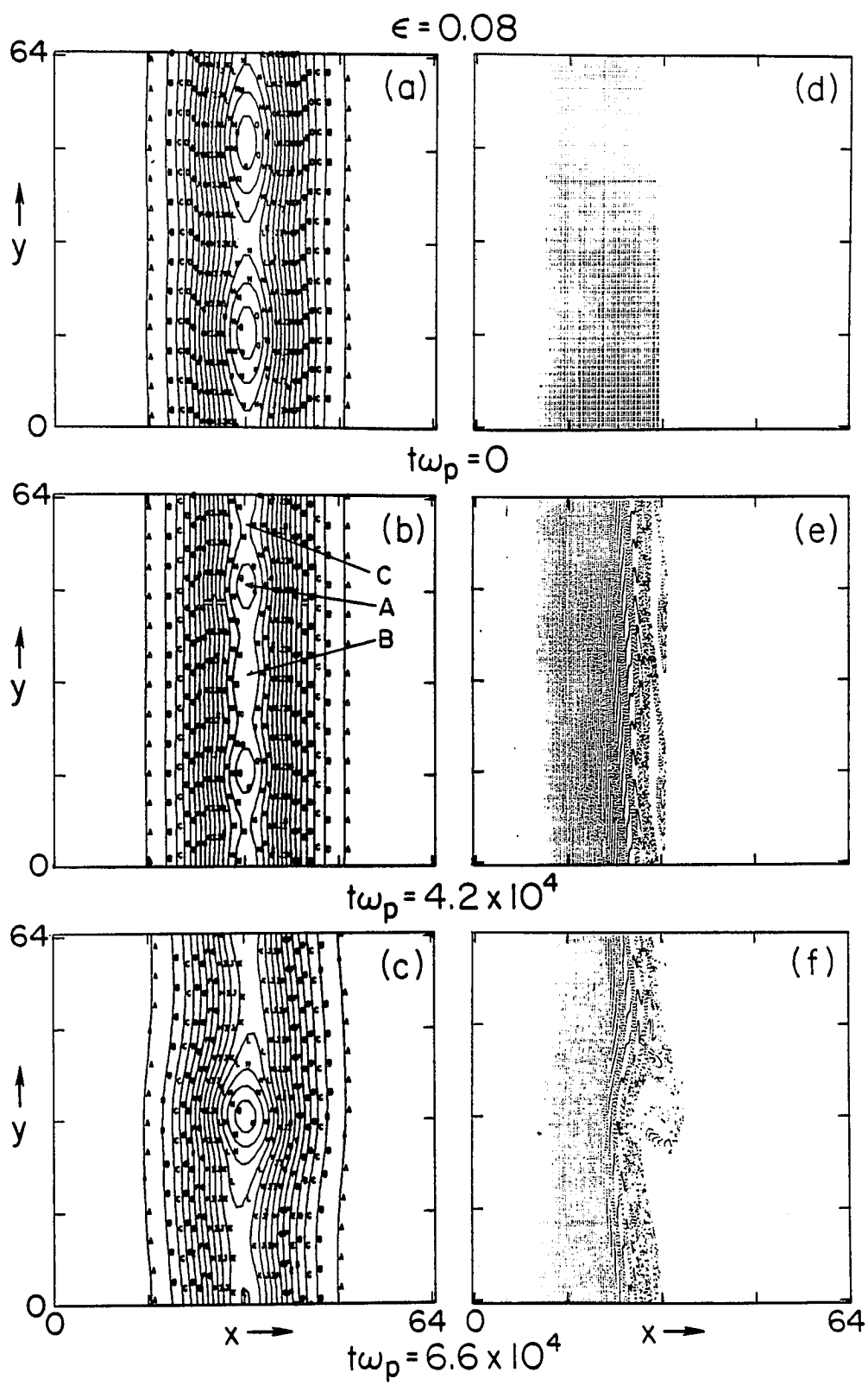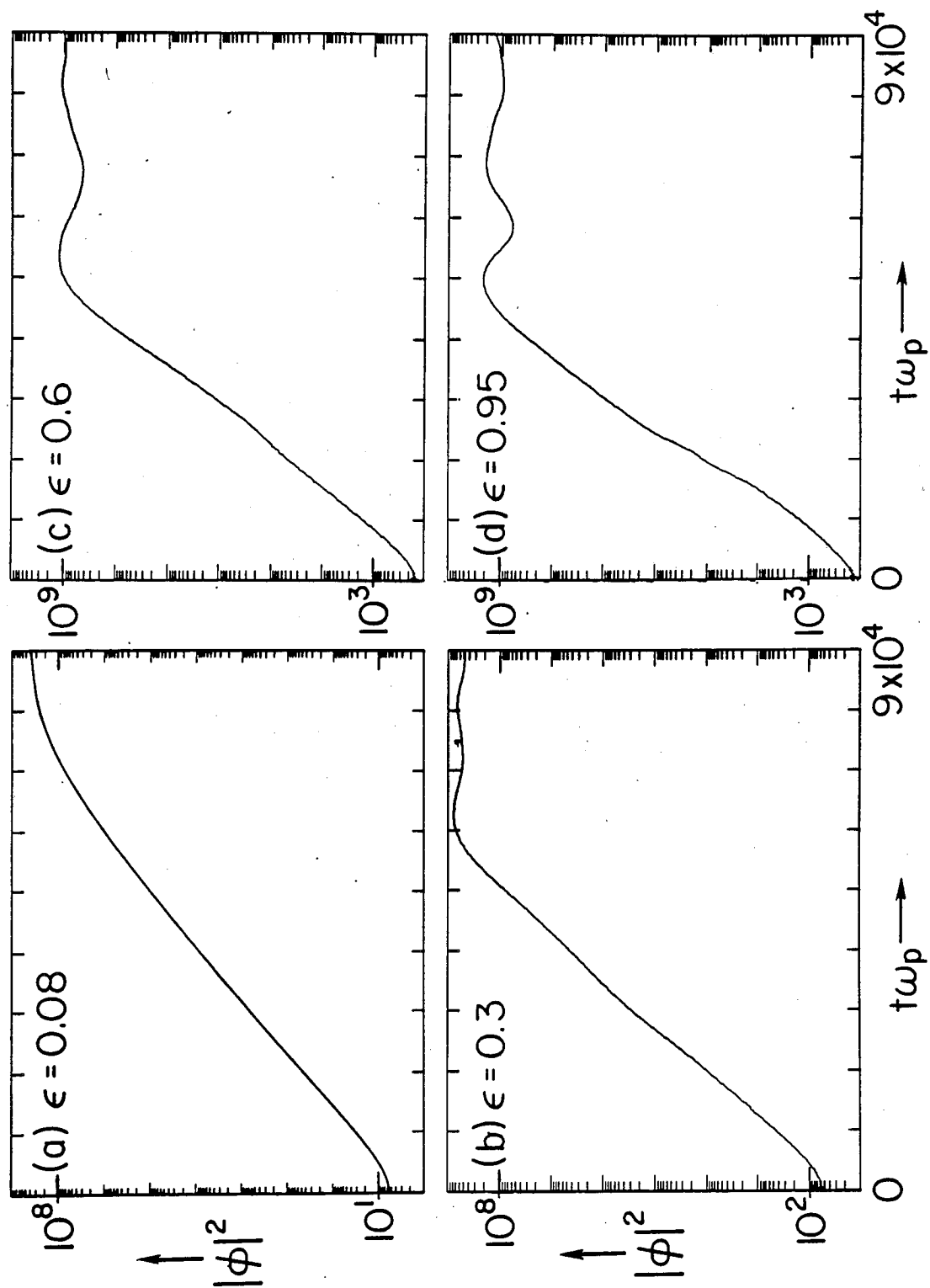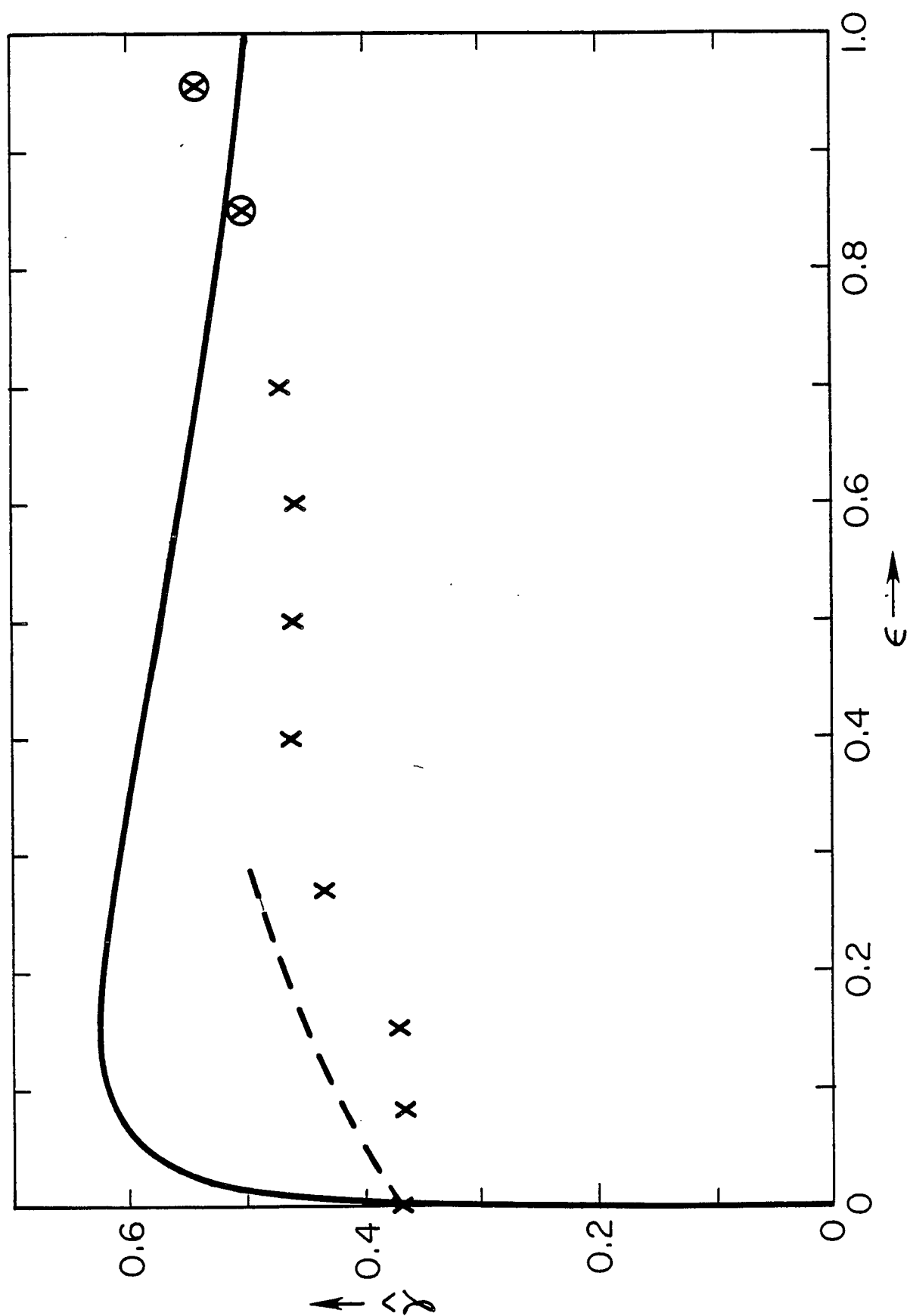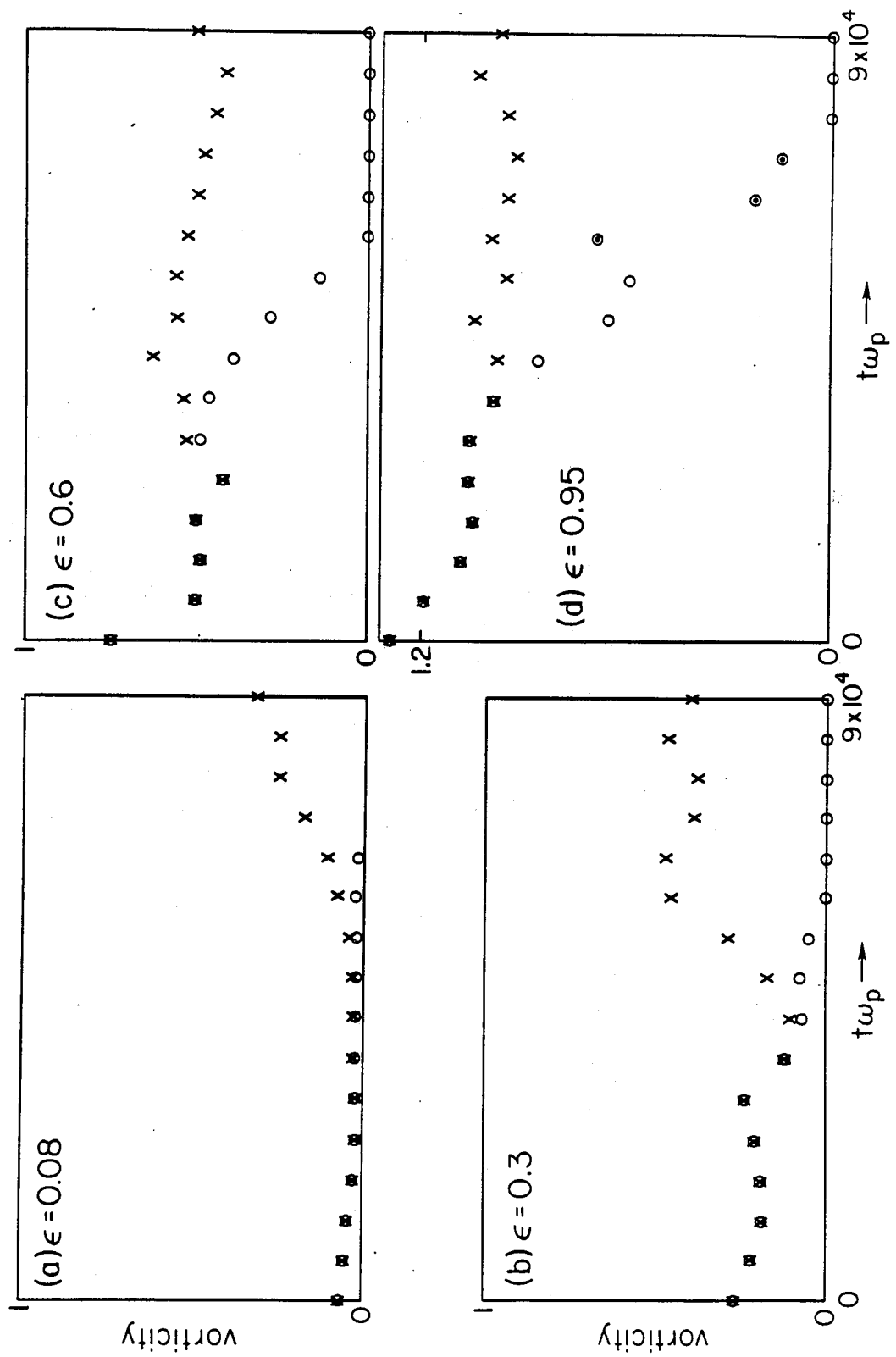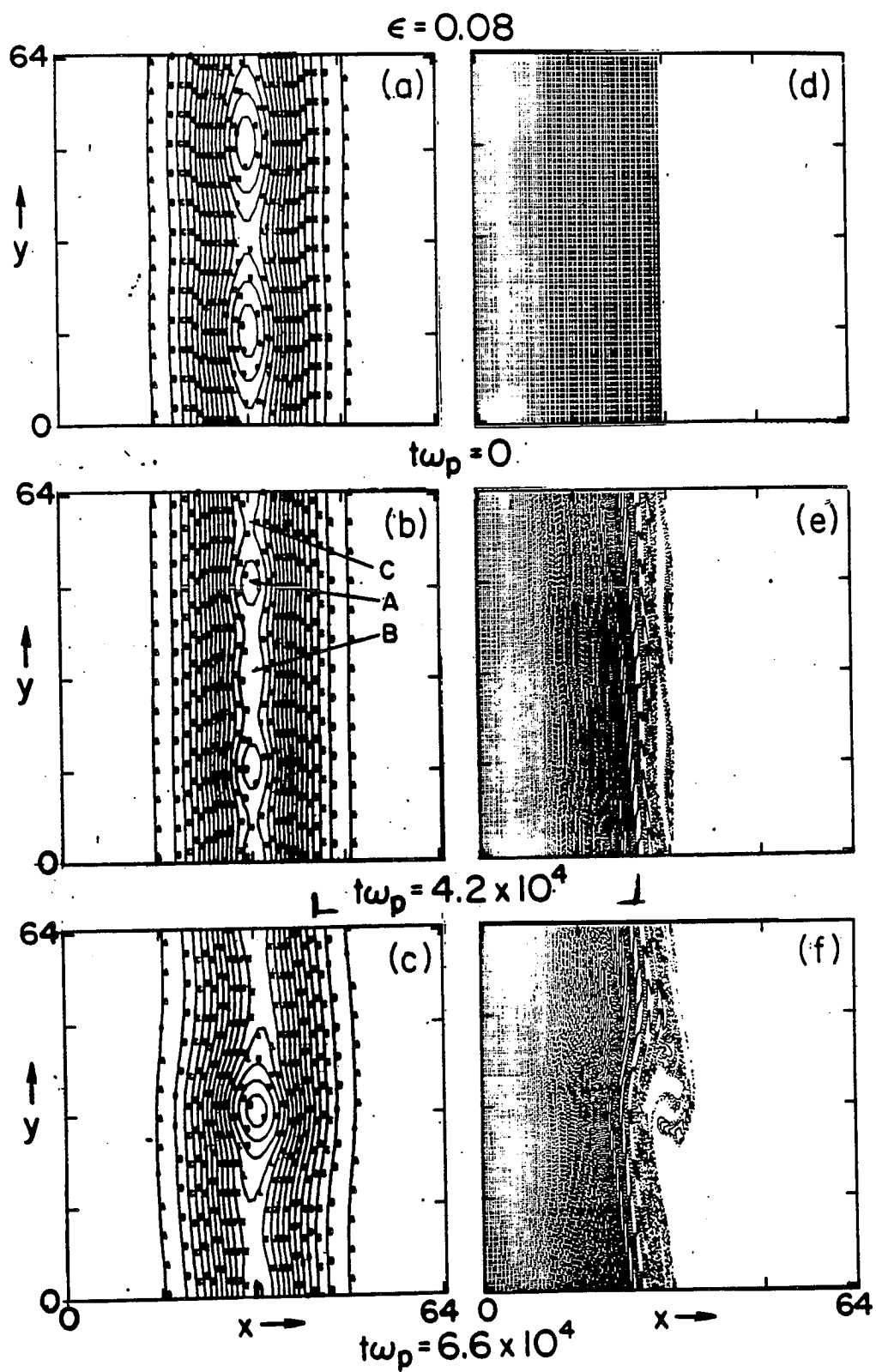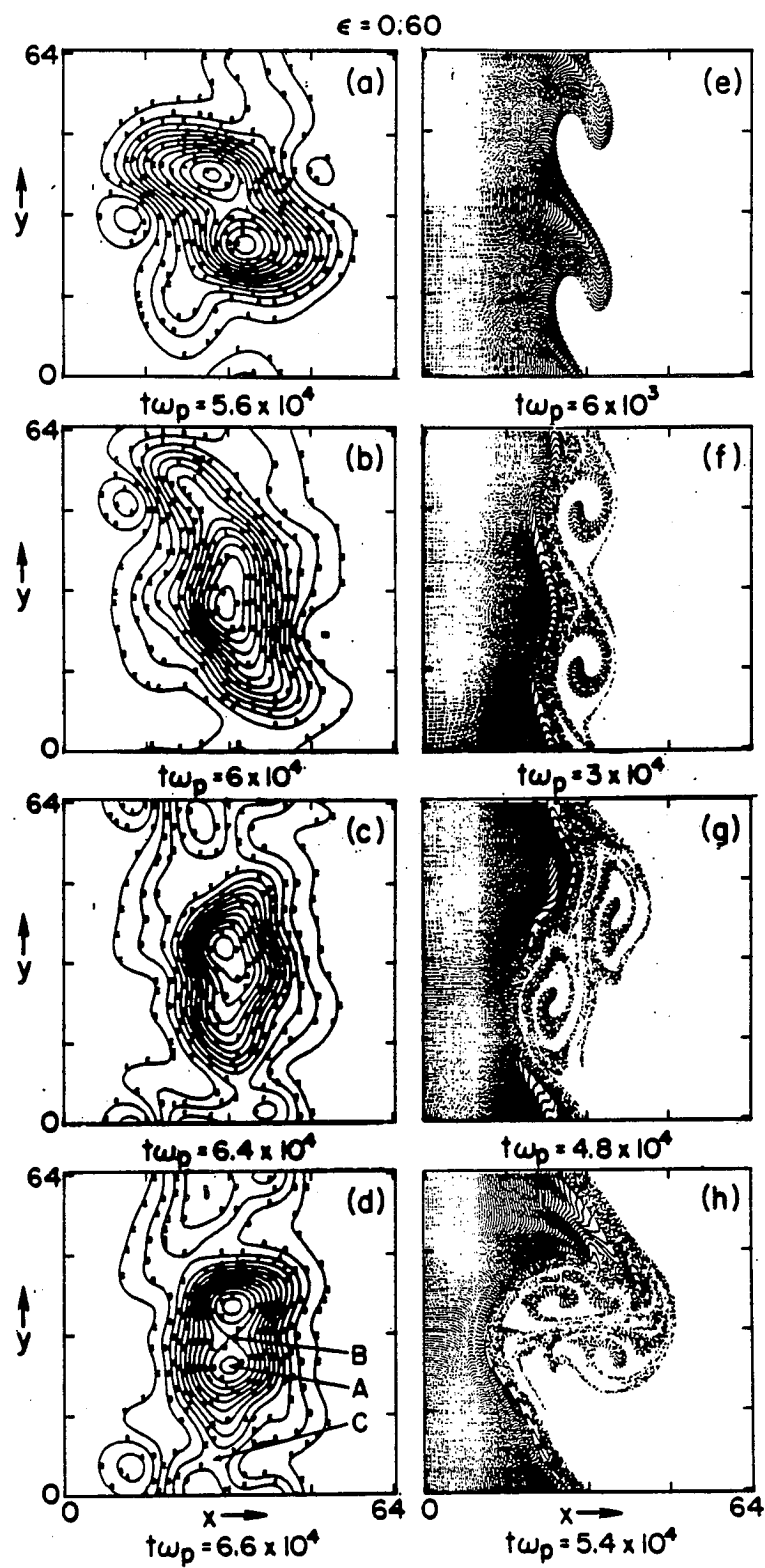
FIG. 12

FIG. 13

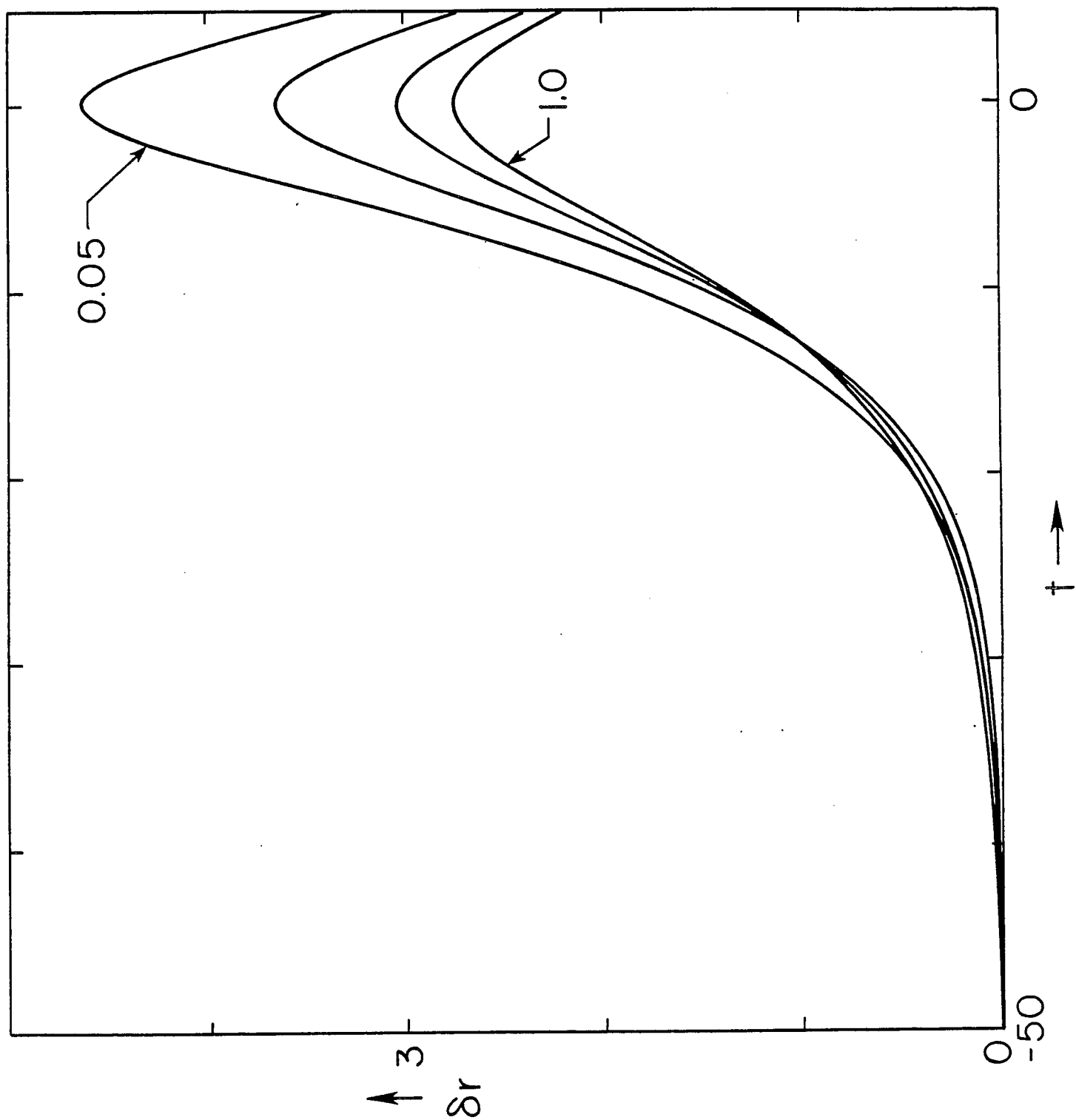FIG. 14

FIG. 15

$k_o\eta$

$k_o\eta$

$k_o\xi$ $k_o\xi$
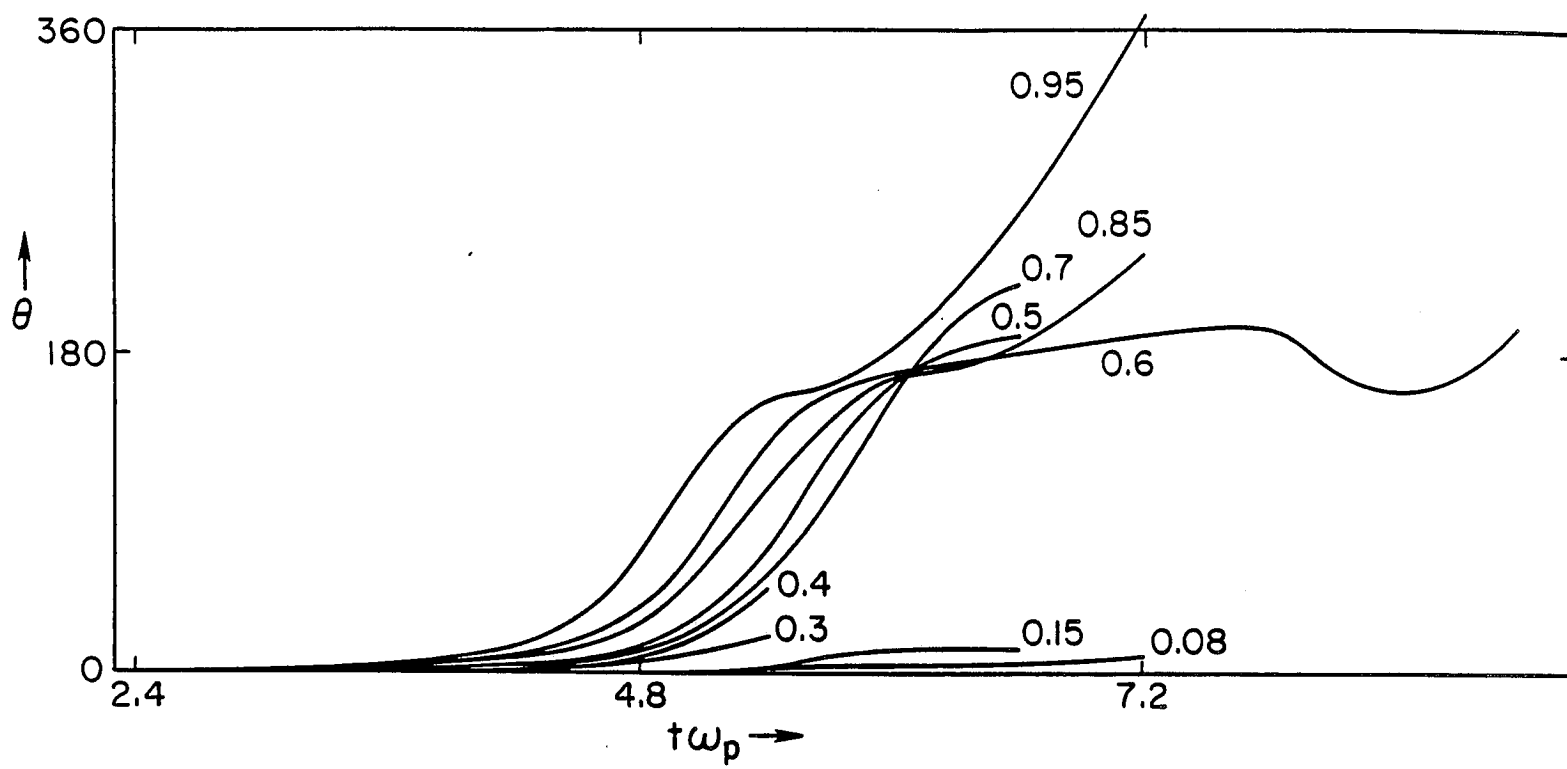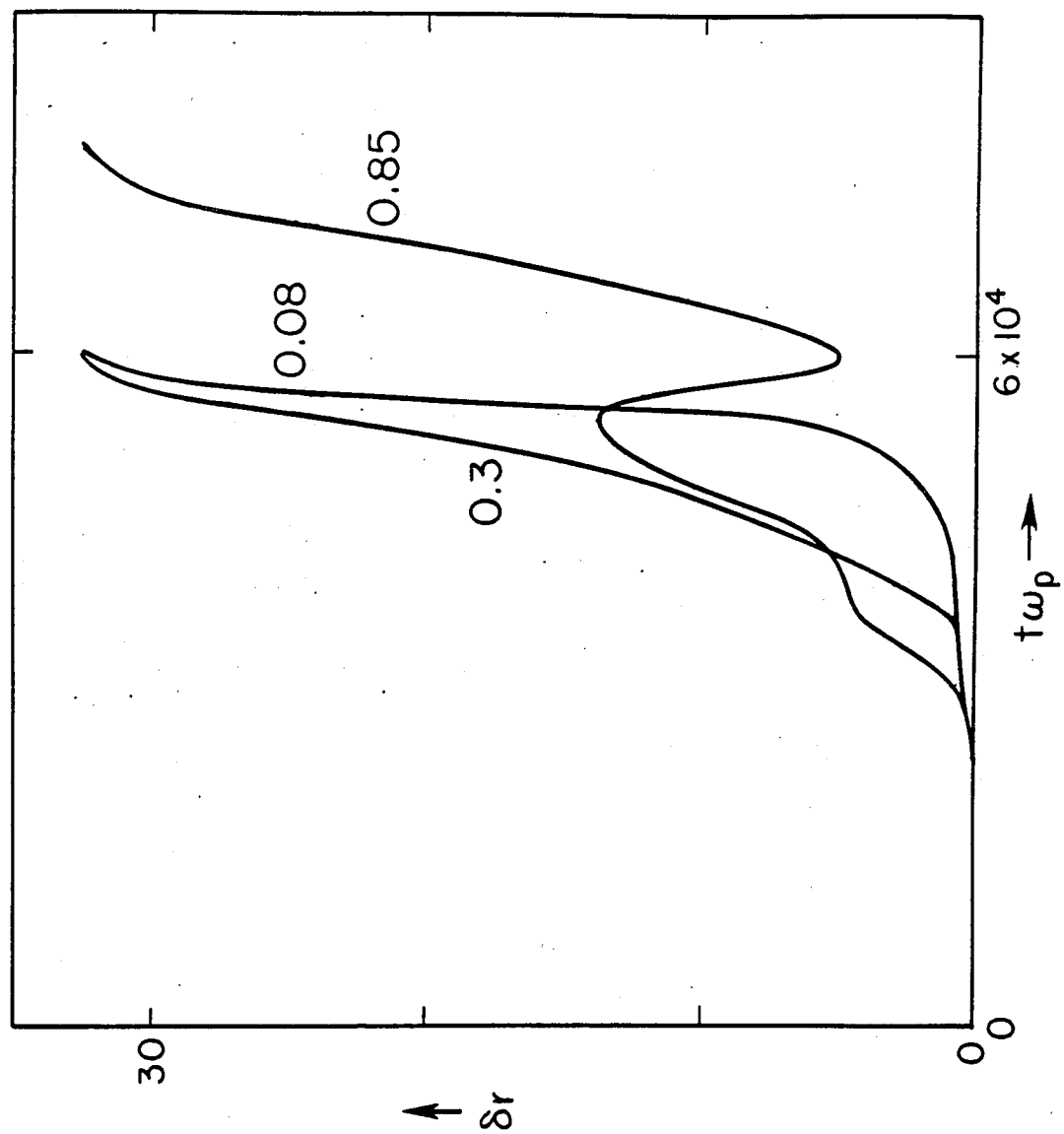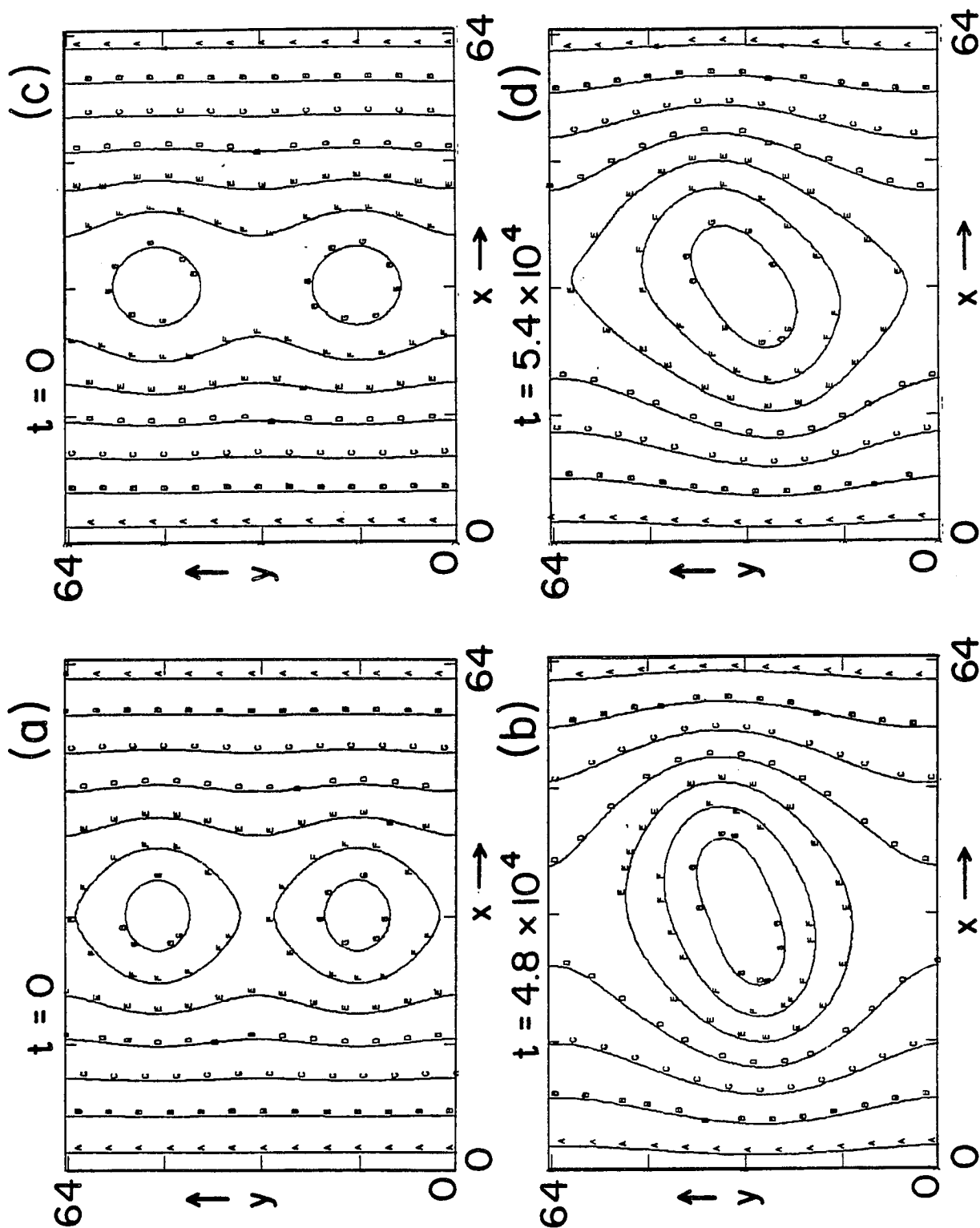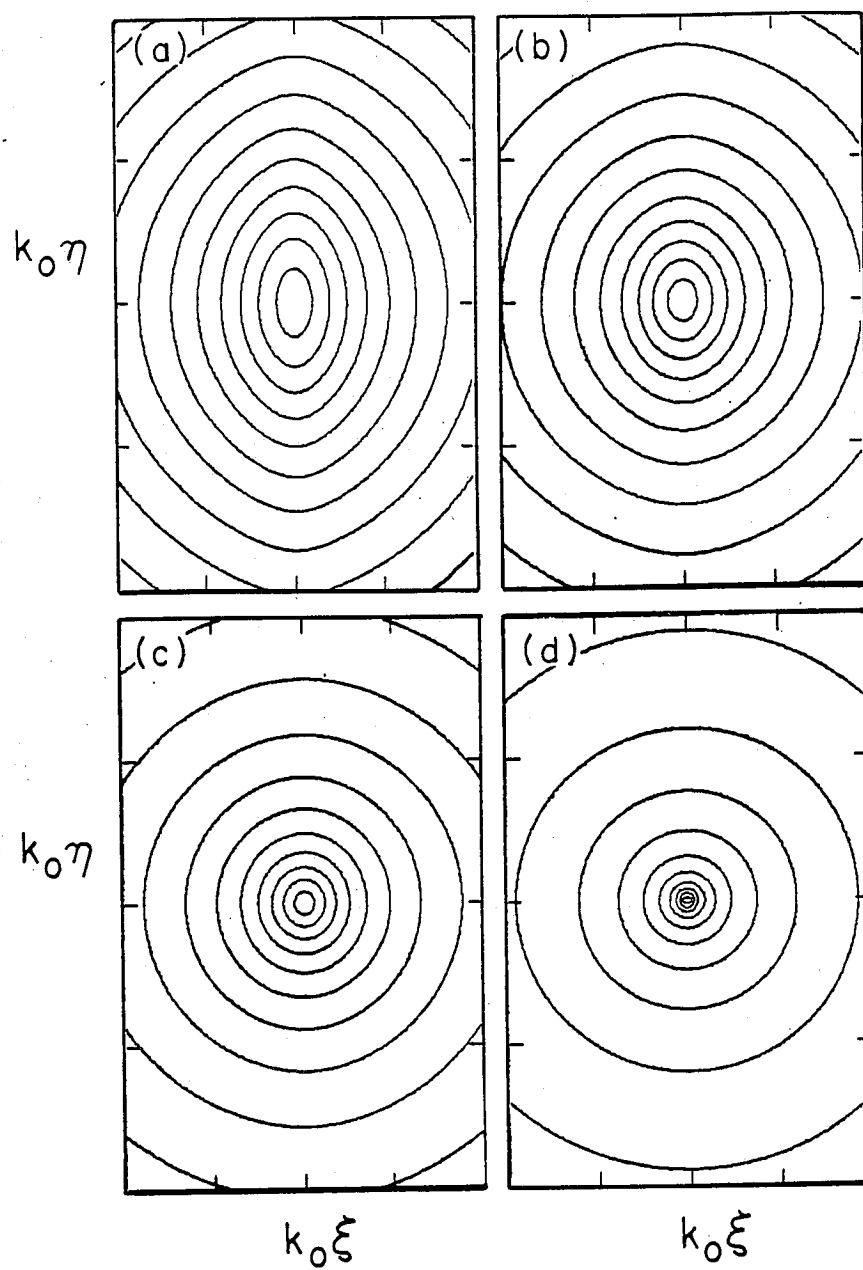
FIG. 16
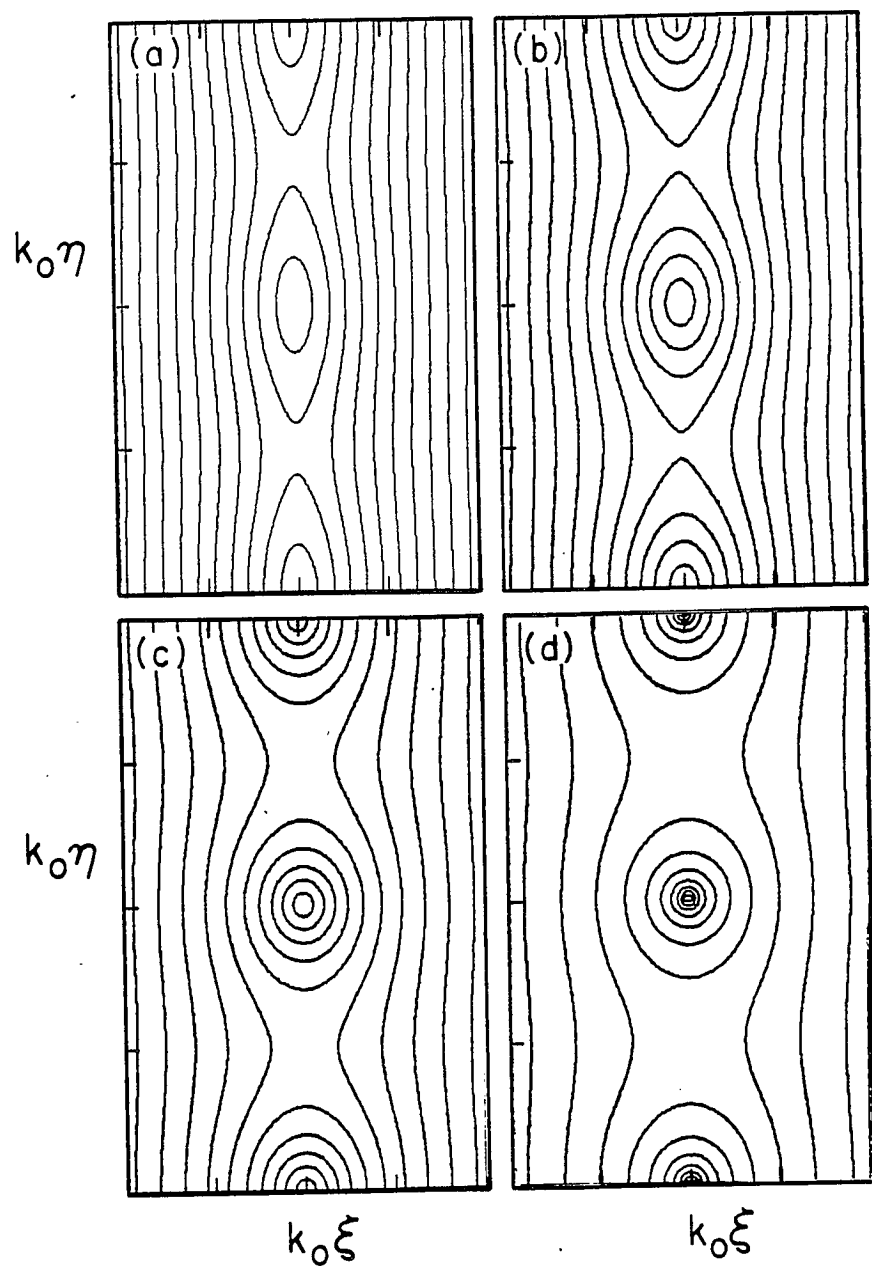
FIG. 17
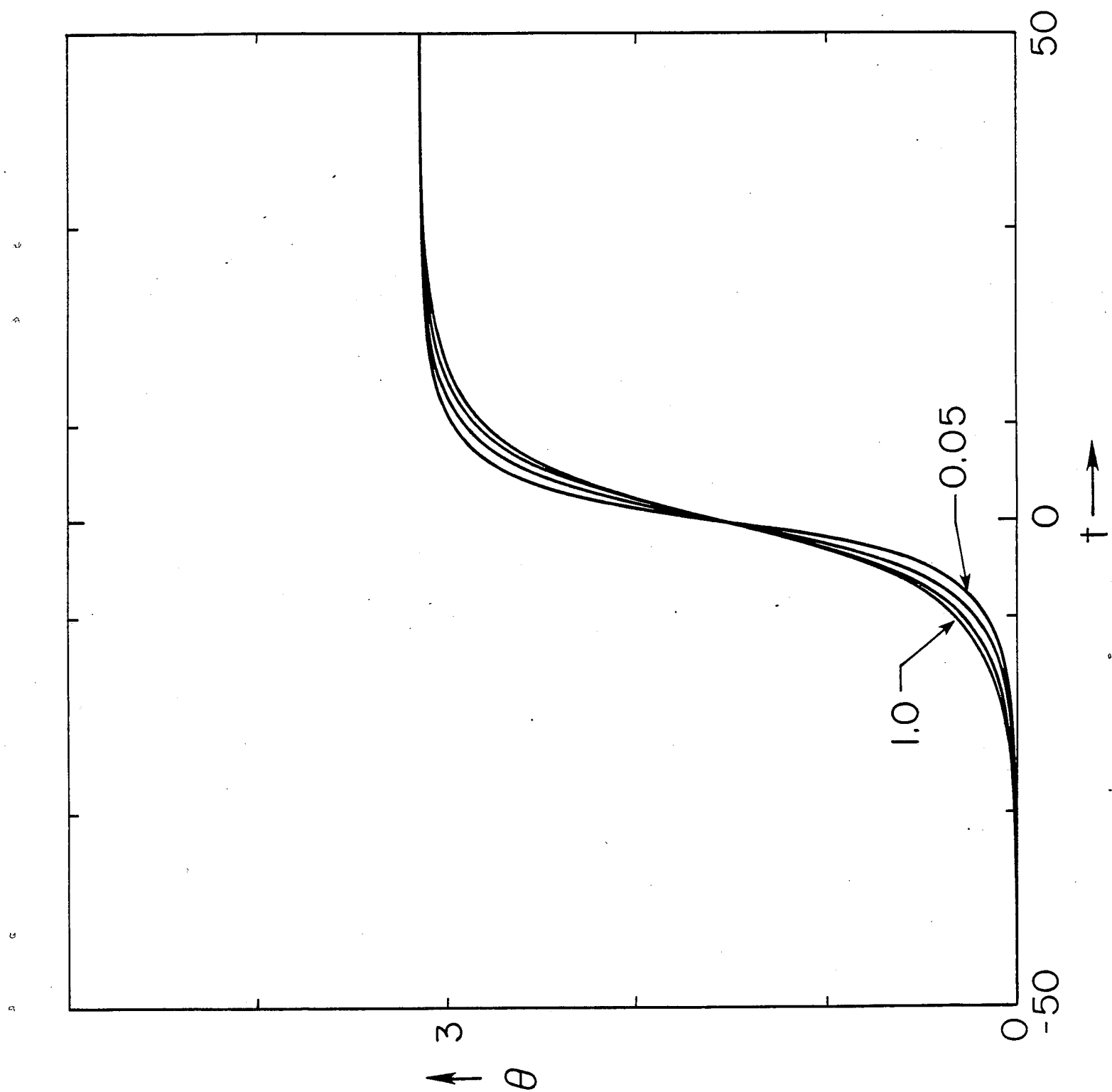
FIG. 18(a)

FIG. 18(b)

FIG. 18(c)

FIG. 18(d)